Study of temporal variations of nitric oxide in the mesosphere and lower thermosphere over Syowa station, Antarctica

Yasuko Isono

Graduate School of Science
(Solar-Terrestrial Environment Laboratory)

Nagoya University

Doctor of Philosophy

2014

Abstract

Energetic particle precipitation (EPP) reach altitudes in Earth's atmosphere that depend on their energies, and disturb the chemical composition such as nitrogen oxides (NO_x = NO+NO_2) in the upper stratosphere, mesosphere and lower thermosphere at the polar region. The increase of NO_x concentration leads the ozone depletion in the mesosphere and upper stratosphere. NO_x has the important role of the chemical composition in the polar upper stratosphere, mesosphere and lower thermosphere.

We have therefore carried out a new ground-based observation at Syowa Station in Antarctica because ground-based observations are best suited to investigate the temporal variation within a localized region. We used the millimeter-wave spectroscopic radiometer which received millimeter-wave radiation emitted by rotational transitions of polar molecules.

We obtained 197 and 172 daily NO spectra in 2012 and 2013 [until 30 September; day of year (DOY) 273], respectively. Most daily NO spectra had a narrow FWHM which is 0.5 MHz, and we could not retrieve the vertical profile by using the pressure-broadening relationship. From the NO spectrum line shape and NO column density relationship with solar radiation, we concluded that the NO was emitted in the altitude range between 75 km and 105 km.

We report temporal variations of the partial column density of nitric oxide (NO) in an altitude range 75–105 km at Syowa Station, Antarctica, from January 2012 to September 2013. We found two patterns of NO temporal variation: (1) a seasonal cycle with a maximum in winter and a minimum in summer, and (2) short-term enhancements on a timeframe of 5–10 days associated with solar activities. In the seasonal cycle, the variation pattern of NO showed good agreement with scotoperiod of solar radiation rather than the downwelling atmospheric transport, suggesting that photo-dissociation is main driver of the seasonal variation. To study the short-term enhancements, we compared the NO column density with the proton and electron fluxes obtained by Polar Orbiting

Environmental Satellite/Meteorological Operational (POES/METOP) satellites. There is a weak but significant correlation between the NO and the electron flux, but no correlation between the NO and the proton flux. We also made detailed comparison of the time series of NO and proton/electron fluxes for 12 selected 25-day timeframes, and found that at least 2 remarkable NO enhancements occurred without any solar proton events (SPEs). During electron precipitation, the NO column density peaked 1–5 days after the commencement of geomagnetic storms, whereas the relationship between the NO and the solar proton is not clear because the electron flux also increased at the same time. These results suggest that energetic electron precipitation may be a major cause of NO enhancements above Syowa station in the auroral region, even during SPEs.

A large geomagnetic storm in April 2012 was very simple and typical single event in which the NO column density began to increase during the recovery phase and peaked on DOY 119 in 2012, which was 4 days after the main phase of the storm. In addition to variations on a timeframe of several days, we found diurnal variations. The increase of NO was related to precipitated electrons in the energy range of 30–300 keV observed by POES/METOP. We found a rapid response and a one-to-one correspondence between them. For the first time we show that a remarkable increase of the column density of NO is caused by dawn-dusk asymmetry of the plasma sheet electrons.

Acknowledgments

This study was carried out in my Ph.D. course at the Solar-Terrestrial Environment Laboratory (STEL), Nagoya University and was achieved under the supervision of Professor Akira Mizuno. I would like to express my great gratitude to Professor Akira Mizuno, my research supervisor, for his patient guidance, encouragement and useful critiques of this study.

I would like to express my sincere gratitude to the members of the advisory committee of my thesis in STEL, Professor Yutaka Matsumi, Associate Professor Tomoo Nagahama, and Associate Professor Yoshizumi Miyoshi of STEL for their fruitful discussion and comments.

I would like to express my gratitude to Assistant Professor Tac Nakajima, Dr. Hirofumi Oyama and Assistant Professor Tomoki Nakayama of STEL, Dr. Toshihisa Kuwahara of Nagoya University, and Associate Professor Hiroyuki Maezawa of Osaka Prefecture University for their guidance, encouragement, discussion and comments during daily Ph.D. course study.

I would like to express my deep appreciation to Professor Takuji Nakamura, Associate Professor Masaki Tsutsumi and Assistant Professor Mitsumu K. Ejiri of National Institute of Polar Research (NIPR) for great support, cooperation, management and encouragement. I felt reassured by their warm support for observation at Syowa Station through more than 1 year.

I also would like to express my appreciation Associate Professor Ryuho Kataoka of NIPR and Professor Hitoshi Fujiwara of Seikei University for their fruitful discussion, comments and encouragement. I improved about the data analysis and writing the manuscript with their cooperation.

I thank the members of the 52nd Japanese Antarctic Research Expedition from the bottom of my heart. I give acknowledgement to the 52nd JARE Leader, Professor Takashi Yamanouchi, and the 52nd JARE Wintering Leader/Station

Manager Mr. Hitomi Miyamoto for their management. I spent very valuable days at Syowa Station with the wintering team.

This study would not have been possible unless helpful supports from engineering staffs of STEL. I wish to thank to Mr. Noriji Toriyama, Mr. Yasusuke Kojima and Mr. Takayuki Yamasaki of STEL, and Mr. Atsushi Morihira of ULVAC for supports to develop the millimeter-wave spectroscopic radiometer.

Thanks are due to members of division I and all colleagues, in particular, Mr. Hiroshi Sasago, Dr. Reiko Nomura and Ms. Mai Ouchi for their supports and encouragement during my Ph.D. cause study.

Finally, I would like to express my deepest gratitude to my family, especially for my parents for their understanding, countless supports and encouragement throughout my life.

This study was supported by the Global COE Program of Nagoya University “Quest for Fundamental Principles in the Universe (QFPU)” from JSPS and MEXT of Japan. This study was also supported by the Leading Graduate schools of Nagoya University “Leadership Development Program for Space Exploration and Research” from JSPS and MEXT of Japan.

Contents

List of Figures

List of Tables

Chapter 1

Introduction

1.1 General Introduction

The Sun sometimes causes huge explosions such as solar flares and the coronal mass ejections, and energetic particles are emanated in substantial amounts associated with these explosion events. These energetic particles are called 'Solar Energetic Particles (SEP)' which consists of protons, electrons and heavy ions in the energy range from a few tens of keV to GeV. SEP can gain direct access to the Earth's atmosphere in polar region with roughly magnetic latitude $\Lambda > 75°$, guided by magnetic field lines, which are basically open near the poles [*Brasseur and Solomon*, 2005].

At the geospace, in contrast, the energetic electrons which cover a wide energy range from a few eV to a few MeV exist. During geomagnetic disturbed periods such as stbstorms and storms, low-energy electrons in the energy range from 1 keV to 10 keV precipitate from the magnetosphere into the Earth's atmosphere in the auroral zone with roughly magnetic latitude $70° < \Lambda < 75°$. High-energy

electrons in the energy range from 10 keV to a few MeV also precipitate from the inner magnetosphere and/or plasma sheet into subauroral zone with roughly magnetic latitude $\Lambda<70°$ [*Brasseur and Solomon*, 2005; *Miyoshi et al.*, 2008; *Horne et al.*, 2009; *Lam et al.*, 2010].

Energetic particle precipitation (EPP) such as SEP and energetic electrons reach altitudes in Earth's atmosphere that depend on their energies as shown in Figure 1.1 [*Turunen et al.*, 2009], and disturb the chemical composition in the upper stratosphere, mesosphere and lower thermosphere at the polar region. EPP lose their energy by collision reactions with the most abundant species such as N_2, O_2 and O in the mesosphere and lower thermosphere. The primary interactions leading to composition changes in the mesosphere and lower thermosphere region are dissociation and dissociative ionization of N_2 and O_2 as well as ionization of N_2, O_2 and O.

$$N_2 + p \rightarrow N + N + p \quad (1.1)$$

$$N_2 + p \rightarrow N + N^+ + p + e \quad (1.2)$$

$$N_2 + p \rightarrow N_2^+ + p + e \quad (1.3)$$

$$O_2 + p \rightarrow O + O + p \quad (1.4)$$

$$O_2 + p \rightarrow O + O^+ + p + e \quad (1.5)$$

$$O_2 + p \rightarrow O_2^+ + p + e \quad (1.6)$$

$$O + p \rightarrow O^+ + p + e \quad (1.7)$$

where p is the incident particle [e.g. *Sinnhuber et al.*, 2012; *Fuller-Rowell*, 1993]. Following the primary interactions, atomic nitrogen, atomic oxygen and ions contribute toward neutral and ionic reactions to change abundance of minor molecules such as nitrogen oxides ($NO_x = NO+NO_2$).

The increase of NO_x concentration leads the ozone depletion in the mesosphere and upper stratosphere. Therefore, NO_x has the important role of the chemical composition in the polar upper stratosphere, mesosphere and lower thermosphere.

1.2 Direct effect of NO_x variation

1.2.1 Solar Proton Event

We introduce the direct effect of NO_x variation due to EPP in this section. When the proton flux with energies >10 MeV reaches more than 10 particles cm^{-2} s^{-1} str^{-1}, we generally call 'Solar Proton Event (SPE)'. SPEs occur sporadically, especially during the solar maximum of the solar cycle, and directly enhance NO concentrations for several days.

Many satellite observations during the solar maximum of solar cycle 23 revealed the spatial and temporal evolution of EPP effects. During the SPE of October 2003, the so-called "Halloween" SPE, a flux of >10 MeV protons observed by GOES-11 satellite were greater than 10^4 particles cm^{-2} s^{-1} str^{-1}. This SPE causes drastic and in-situ increases of NO_x concentration. Arctic mean increase of NO_x concentration was between 20 ppbv to 70 ppbv with altitudes 40-60 km, and the Antarctic mean increase NO_x concentration was between 10 ppbv and 35ppbv as shown in Figure 1.2 [*López-Puertas et al.,* 2005]. Figure 1.2 shows NO_x and ozone concentration during the Halloween event, and we find that increase of NO_x concentration is spread not only the polar region with geomagnetic latitude Λ >75° but also the region with geomagnetic latitude Λ >60°.

During the solar maximum of solar cycle 23 several large SPEs occurred, and several studies reported NO_x enhancements and associated depletions of ozone [e.g., *Jackman et al.*, 2001, 2005, 2011; *Verronen et al.*, 2005; *Seppälä et al.*, 2006]. These also spread the region of increase of NO_x concentration with geomagnetic latitude Λ >60°.

Recently, *Jackman et al.* [2013] reported the NO_x changes caused by the SPE during January and March 2012, that is, during the solar maximum of solar cycle 24. As shown in Figure 1.3, a flux of >10 MeV protons observed by GOES satellite were greater than 10^3 particles cm^{-2} s^{-1} str^{-1} during both SPE, and high ionization rate calculated by profiles of proton flux were expand in the altitude range between 60 km and 80 km with geomagnetic latitude Λ >60°. According the 2-D model (Figure 1.4b and 1.4d), the NO_x reached more than 50 ppbv in the southern polar mesosphere between 60° and 90° around DOY 25 and 69. However, the Envisat Michelson Interferometer for Passive Atmospheric Sounding (MIPAS) observations indicated a small NO_x increase by < 20 ppbv and by >10 ppbv for only several days in January and March 2012, respectively.

By using satellite observations, it was revealed that the SPE widely influenced the direct effect of NO_x variation in the polar region with geomagnetic latitude >60°.

1.2.2 Energetic Electron Precipitation

Electrons from the inner magnetosphere and/or plasma sheet also directly enhance NO concentrations for several days. A precipitation of electrons is often occurred during the geomagnetic disturbance periods.

The Student Nitric Oxide Explorer (SNOE) satellite observes the variation of nitric oxide (NO) in the lower thermosphere. In the case of auroral electrons with energies of 1–10 keV, *Solomon et al.* [1999] found a correlation between auroral activity and the NO variability in the lower thermosphere at the magnetic latitudes between 45° and 70° in the both hemispheres. They discussed the fact that heating of the atmosphere is an important mechanism of NO production as well as direct particle impact. *Baker et al.* [2001] and *Barth et al.* [2003] show time series of the daily averaged NO density in the magnetic latitude between 60° and 70° measured by SNOE at 106 km altitude in both hemispheres between 1998 and 2000. They have found that correlation coefficients of 0.56 (north) and 0.73 (south) for NO density versus electron count rates with energies > 25 keV observed by the Solar, Anomalous, and Magnetospheric Particle Explorer (SAMPEX). The widely influence of the energetic electron precipitation became clear by satellite observations.

Compared to such satellite observations, ground-based observations are best suited to investigate in detail the temporal variations caused by the EPP within a localized region. For example, *Newnham et al.* [2011] used continuous measurements at Troll station in Antarctica to reveal the direct production of NO in the upper mesosphere by electrons with energies of ~300 keV as shown in Figure 1.5. That electron precipitated from the outer radiation belt during the moderate geomagnetic storm. In addition, *Newnham et al.* [2013] show enhanced mesospheric NO concentration in winter 2008 which is solar minimum of the solar cycle 24 at Troll station in Antarctica. During this period, some geomagnetic storm occurred, but these classes were weak or moderate. They suggest that the NO may be produced directly in the mesosphere in altitude range between 65 km and 80 km by electrons in energy range > 200 keV or originate from a source at

higher altitudes.

In addition the widely observation by using satellite, it is important to investigate the temporal variations due to EPP within a localized region by using ground-based observations. However, at present time satellite observations outnumber such ground-based studies.

1.3 Indirect effect of NO_x variation

Next, we describe the indirect effect of NO_x variation due to atmospheric transport. This indirect effect originates the EPP in the lower thermosphere, although NO_x variation occurs in the mesosphere and stratosphere.

The stratosphere and mesosphere have characteristic meridional transport. In the lower stratosphere, that is the Brewer-Dobson circulation which circulates from low latitude in the tropopause to high latitude in the lower stratosphere. This circulation has strong seasonal trend. Above the middle stratosphere, on the other hand, a meridional transport occurs from the summer pole to the winter pole. This circulation reaches in the altitude range about 90 km using by the Whole Atmosphere Community Climate Model (WACCM) [*Smith et al.*, 2011]. Therefore, a downward flow occurs between the stratosphere and mesosphere in the winter pole. In addition, polar vortex which is a persistent, large-scale cyclone is formed in the polar stratosphere during winter. It isolates the inside atmosphere of polar vortex, and downward flow is kept inside of polar vortex.

The NO which enhanced in the lower thermosphere comes down into mesosphere and upper stratosphere due to polar vortex during winter. NO produced in the lower thermosphere descends into the mesosphere and upper

stratosphere because of downward atmospheric transport during the polar winter. The Halogen Occultation Experiment (HALOE) satellite has observed substantial NO enhancement at high latitudes during the winter from the mesopause down to altitudes of about 55–60 km as shown in Figure 1.6a. The latitudes associated with these NO enhancements are 45–55° during the period from 2–6 weeks after the winter solstice and 70–80° during the period from 0–3 weeks after the spring equinox [*Siskind and Russell*, 1996]. It is well known that NO catalytically destroys ozone, and *Daae et al.* [2012] revealed that NO increased by an energetic electron precipitation in late July 2009 caused mesospheric ozone depletion between 60 km and 75 km combined with the atmospheric descending motion. Below the mesosphere, NO is regarded as a form of odd nitrogen, NO_x (= NO + NO_2), because NO rapidly changes to NO_2 by capturing oxygen during the night, and NO_2 returns to NO by photo-dissociation in the daytime by equations (1.12) - (1.15). Enhancement of NO_2 due to downward transport has been revealed by HALOE, ACE-FTS, POAM [*Randall et al.*, 2007, 2009], GOMOS [*Seppälä et al.*, 2007] (Figure 1.6b), and VLF wave propagation data obtained at Iceland, Ny Ålesund, and Érd as a part of Antarctic-Arctic Radiation-belt Dynamic Deposition VLF Atmospheric Research Konsortia (AARDDVARK) combined with an Sodankaylä Ion Chemistry (SIC) model [*Clilverd et al.*, 2007] and so on. Such downward transport of NO_x may cause stratospheric ozone depletion due to the NO_x catalytic cycle. *Seppälä et al.* [2007] observed a significant O_3 decrease in the upper stratosphere that corresponded to NO_x enhancement in the northern polar region, but the hypothesis that there is a direct link between O_3 depletion and downwelling of NO_x should be tested by further modeling. As before, satellite observation is the main observation technique.

1.4 Chemistry of Nitric Oxide in the mesosphere and thermosphere

In this thesis, we focus on NO. We describe neutral and ion-neutral reactions of NO in the mesosphere and thermosphere. From the primary interaction due to EPP (equations (1.1-1.7)), atomic nitrogen, atomic oxygen and ions are produced. The NO is mainly produced by the excited state of atomic nitrogen with molecular oxygen (equation (1.8)). The ground state atomic nitrogen also produces the NO but this reaction is very sensitive to the temperature of the thermosphere (equation (1.9)) [*Brasseur and Solomon*, 2005]. Ions such as O_2^+ and NO^+, which dominate in the lower thermosphere, are rapidly lost below 80 km. Ions (N^+, N_2^+, O^+, O_2^+ and NO^+) and the atomic oxygen react in ion-neutral reactions in the thermosphere (Table 2) [*Fuller-Rowell*, 1993], and relate production for atomic nitrogen.

$$N(^2D) + O_2 \rightarrow NO + O \quad (1.8)$$

$$N(^4S) + O_2 \rightarrow NO + O \quad (1.9)$$

The principal loss process for NO is reaction with the ground state atomic nitrogen.

$$NO + N(^4S) \rightarrow N_2 + O \quad (1.10)$$

Another loss process for NO is the photodissociation.

$$NO + h\nu \rightarrow N(^4S) + O \quad (1.11)$$

Equations from (1.8) to (1.11) are main chemical reaction of NO production and loss [*Brasseur and Solomon*, 2005].

In the mesosphere, these are the major chemical reactions between NO and NO_2 as follows.

$$NO_2 + h\nu\ (244 - 398\ \text{nm}) \rightarrow NO + O \quad (1.12)$$

$$NO_2 + O \rightarrow NO + O_2 \quad (1.13)$$

$$NO + O + M \rightarrow NO_2 + M \quad (1.14)$$

$$NO + O_3 \rightarrow NO_2 + O_2 \quad (1.15)$$

In the altitude range below ~75 km, most NO is converted into NO_2, as shown in equation (1.15), at night, when there is no solar radiation and less of the reactant O. During the day, solar radiation restores the NO as shown in equations (1.12) and (1.13). In contrast, in the altitude range between 75 km and 110 km, there is almost no diurnal variation because the reactions (1.12) and (1.15) are no longer effective due to very small amount of NO_2 and O_3 [*Ogawa and Shimazaki*, 1975]. We summarize the chemistry of NO in the mesosphere and thermosphere in Figure 1.7, although we omit the ion-neutral reactions which do not directly relate production of atomic nitrogen (right column of Table 1.1) in Figure 1.7.

Table 1.1 Ion-Neutral Reactions [*Fuller-Rowell*, 1993]

$N_2^+ + O \rightarrow N(^2D) + NO^+$	$N^+ + O_2 \rightarrow NO^+ + O$
$NO^+ + e \rightarrow N(^2D) + O$	$N^+ + O \rightarrow O^+ + N$
$\rightarrow N(^4S) + O$	$O_2^+ + e \rightarrow O + O$
$N_2^+ + e \rightarrow N(^4S) + N(^4S)$	$O_2^+ + NO \rightarrow NO^+ + O_2$
$\rightarrow N(^4S) + N(^2D)$	$O_2^+ + N(^4S) \rightarrow NO^+ + O$
$N^+ + O_2 \rightarrow O_2^+ + N(^4S)$	$O^+ + O_2 \rightarrow O_2^+ + O$
$O^+ + N_2 \rightarrow NO^+ + N(^4S)$	$NO + h\nu_{\mathrm{Lyman}\alpha} \rightarrow NO^+ + e$

1.5 Purpose of this thesis

The increase of NO_x concentration leads the ozone depletion in the mesosphere and upper stratosphere. Therefore, NO_x has the important role of the chemical composition in the polar upper stratosphere, mesosphere and lower thermosphere. We introduced the effect of NO_x variation due to SPE, energetic electrons and atmospheric transport. Most of these studies observed the NO_x concentration using by satellite, and they focused on single event. Satellite observations are able to investigate a global effect, and they can compare these results with global simulations. However, NO_x variation in the stratosphere, mesosphere and lower thermosphere reflect the net effect of multiple causes such as SPE and energetic electrons and effect of atmospheric transport.

We are interested in quantifying the changes of NO caused by these effects, and

we would like to know how large the influence of these effects is in a timeframe longer than one year in the mesosphere and lower thermosphere. In contrast with satellite observations, ground-based observations are best suited to investigate the temporal variation within a localized region. We have therefore carried out a new ground-based observation at Syowa Station in Antarctica.

In this thesis, we report results of NO observation by using our ground-based millimeter-wave spectroscopic radiometer at Syowa Station in Antarctica The observation period was between January 2012 and September 2013, which coincided with the solar maximum of solar cycle 24. In Chapter 2, we introduce the observation site 'Syowa station in Antarctica'. We also describes details of the millimeter-wave spectroscopic radiometer which receive millimeter-wave radiation emitted by rotational transitions of polar molecules, and observation method which is frequency switching. Chapter 3 shows the NO spectrum at 250.796 GHz, and we describe characteristics of NO spectra for 2 years observation period. The most remarkable feature of the results is that the line widths of the spectra were narrow. From the NO spectrum line shape, we estimate the NO emitting region. We also describe the derivation of the column density of NO because we could not retrieve the vertical profile by using the pressure-broadening relationship. In Chapter 4, we describe the temporal variations of NO in 2012-2013. We found the seasonal variation and the short-term variation of NO for several days. In Chapter 5, we introduce the typical single event in April 2012. During this event, fluxes of electrons with energies >30 keV increased to 10^6 (cm^{-2} s^{-1} str^{-1}), but proton fluxes remained at the noise level. According to high temporal resolution data (3-h-integrated data), we conclude that NO enhancement in this case was affected by electron precipitation.

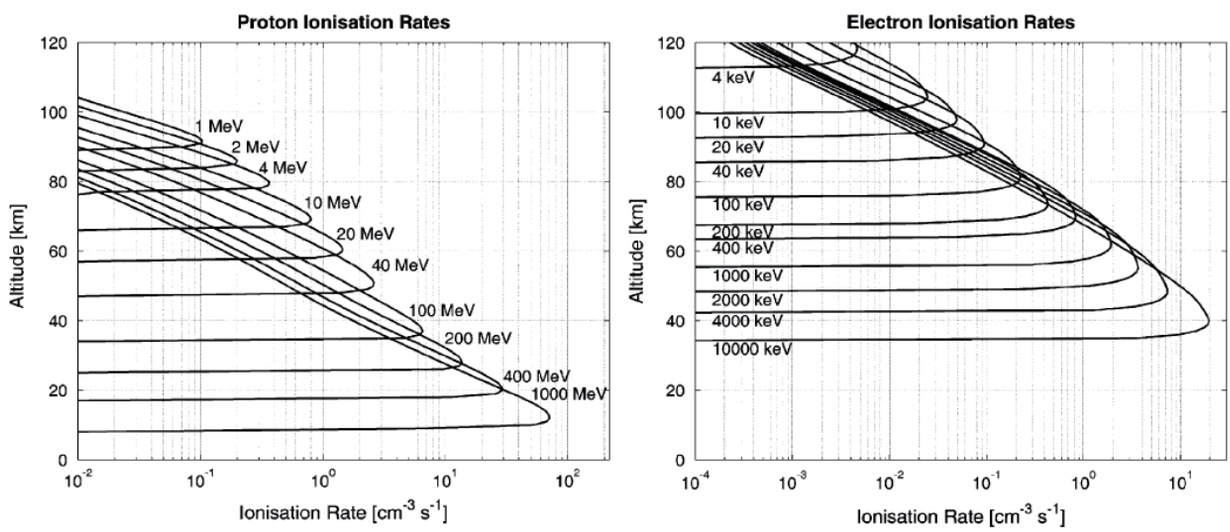

Figure 1.1 Altitude versus ionization rates for mono energetic beams of (left) protons with energies 1-1000 MeV and (right) electrons with energies 4-4000 keV [*Turunen et al.*, 2009].

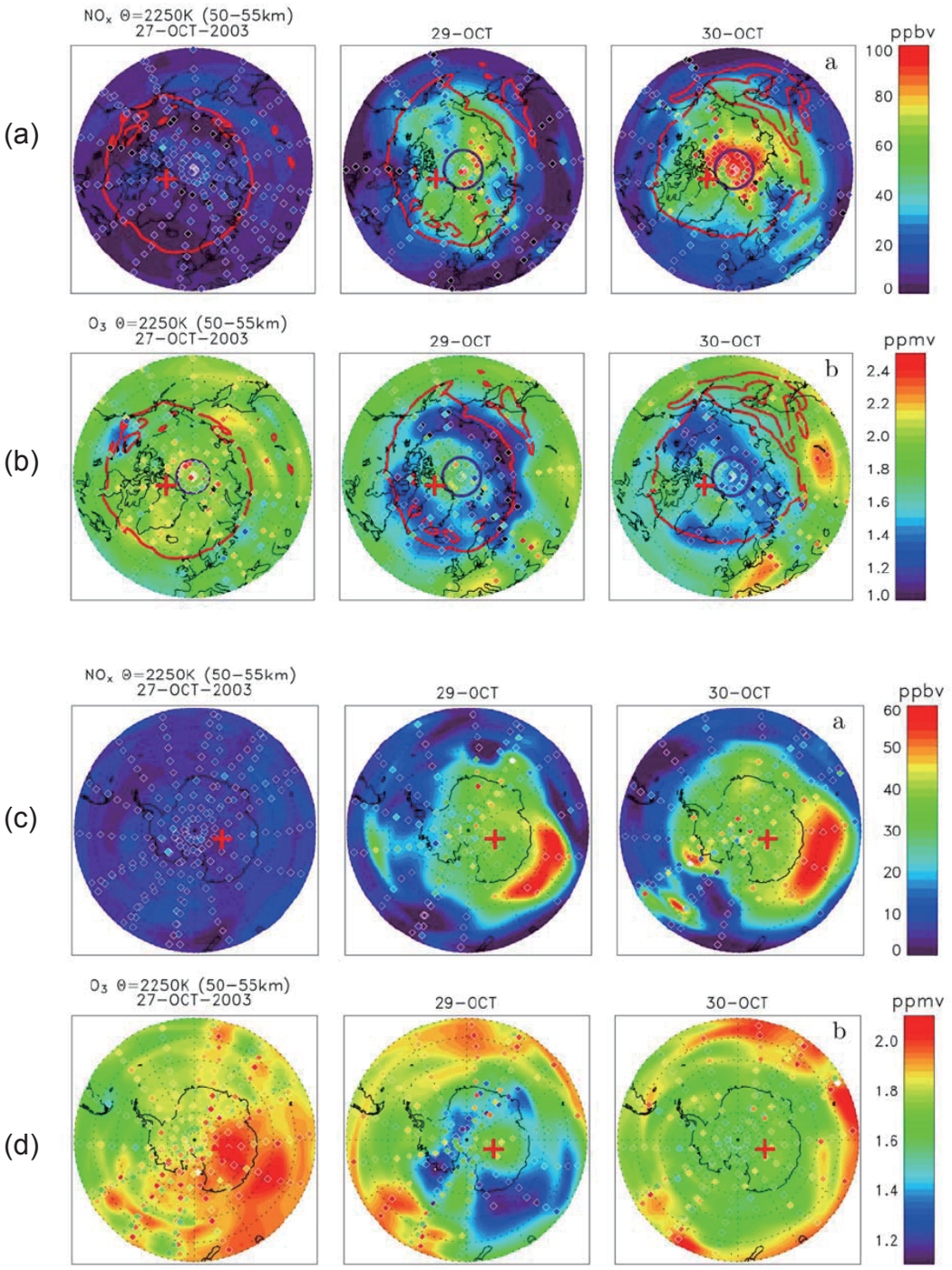

Figure 1.2 (a) NO_X(ppbv) and (b) ozone(ppmv) concentration in the Northern hemisphere for days 27, 29 and 30 October 2003 at a potential temperature level of 2250 K. (c) and (d) are same as (a) and (b), but these are in the Southern hemisphere [*López-Puertas et al.*, 2005].

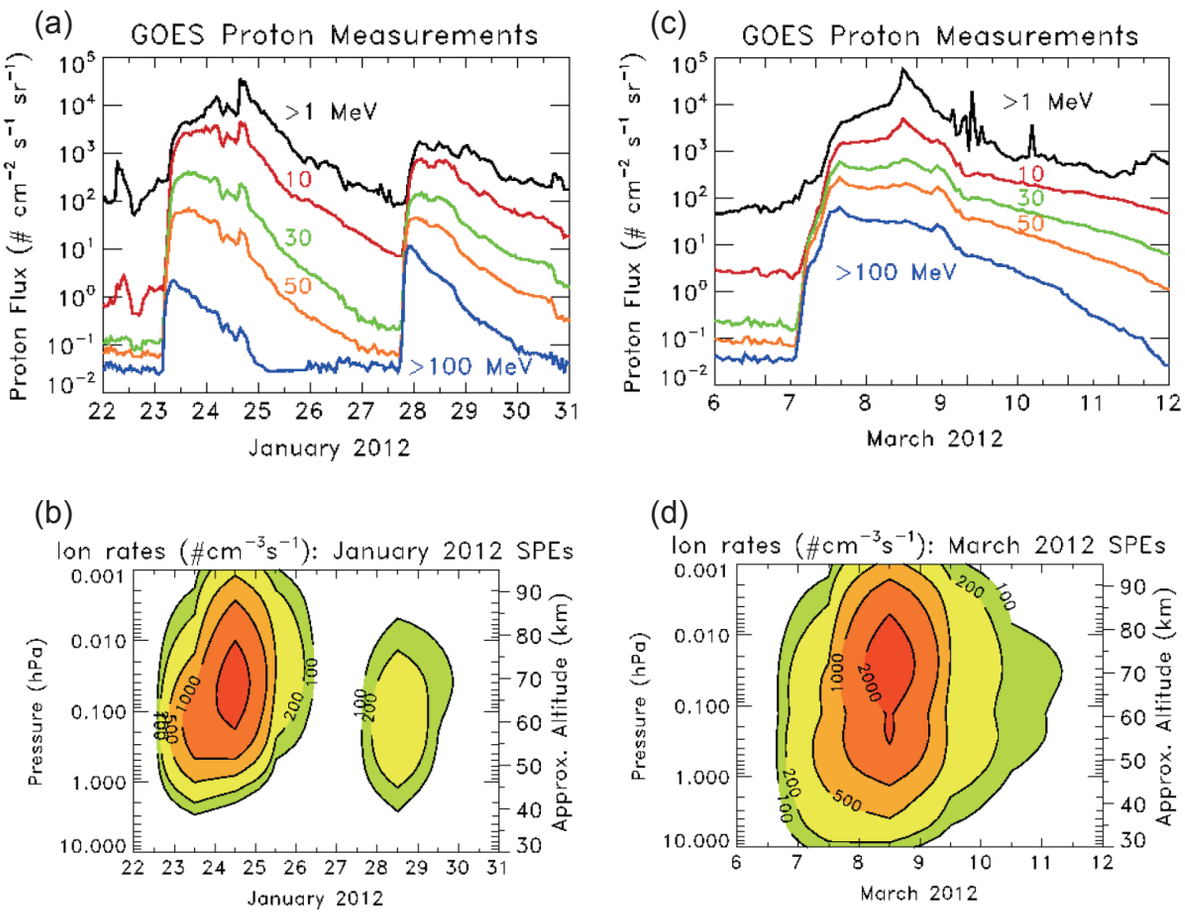

Figure 1.3 (a) and (c) are GOES-13 proton flux measurements in January 2012 and March 2012, respectively, for energies >1 MeV(black), >10 MeV (red), >30 MeV(green), >50 MeV(orange), >100 MeV(blue). (b) and (d) are daily averaged ionization rates over the 10 to 0.001 hPa pressure range for the 22-30 January 2012 time period and for the 6-11 March 2012 time period, respectively [*Jackman et al.*, 2013].

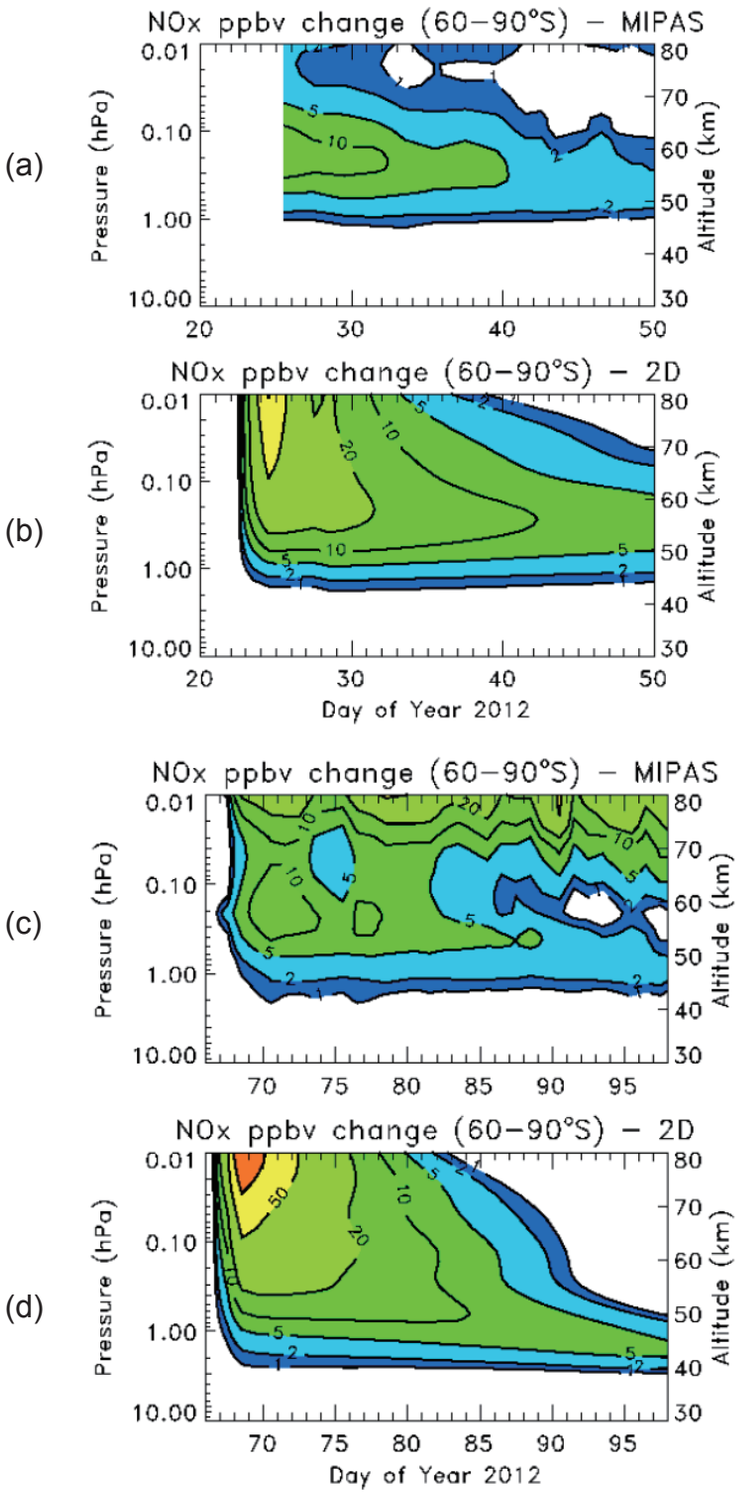

Figure 1.4 Daily averaged NO_x changes in the geomagnetic latitude between 60° and 90° . (a) indicates the results measured by MIPAS and (b) indicates the results calculated by the GSFC 2-D model during SPE in January 2012. (c) and (d) are same as (a) and (b), respectively, but during SPE in March 2012 [*Jackman et al.*, 2013].

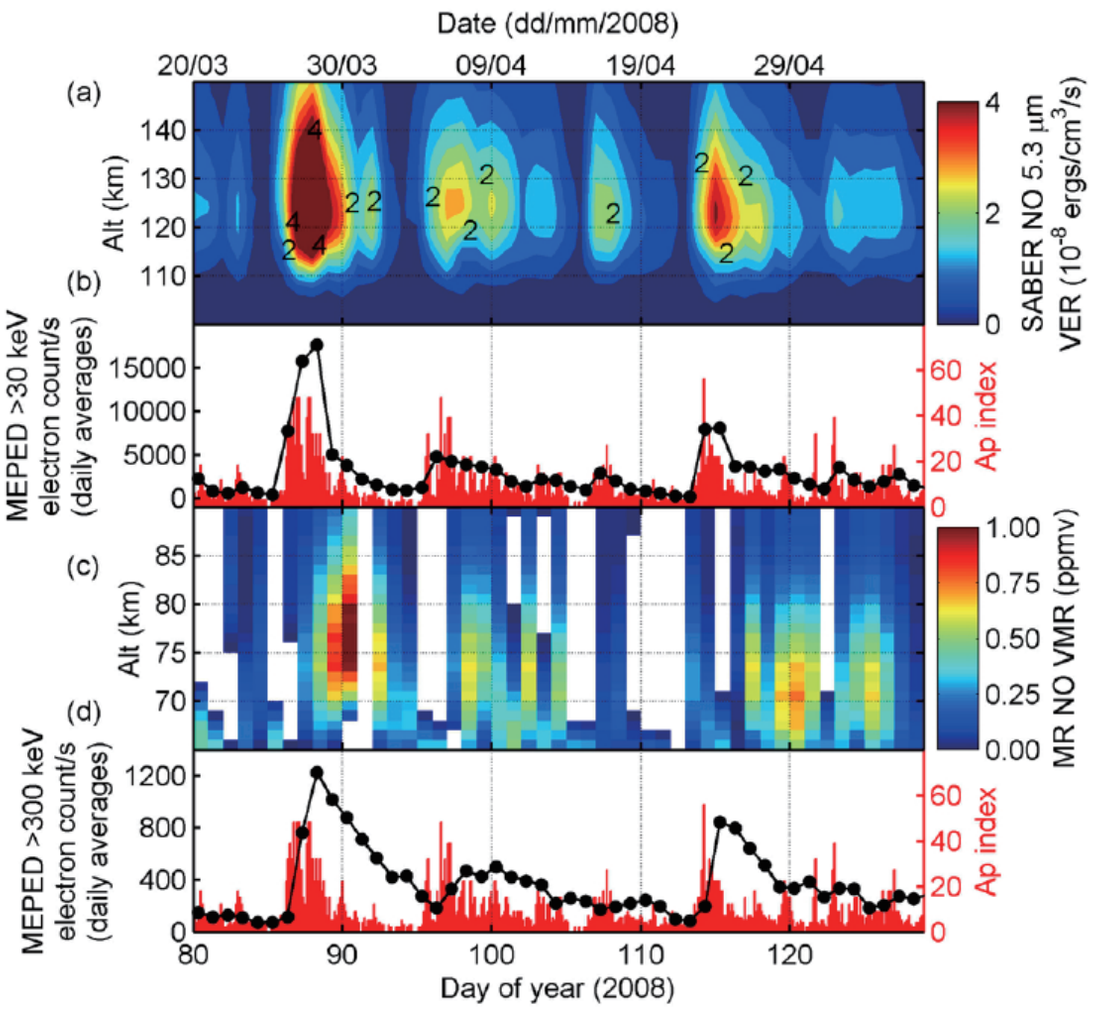

Figure 1.5 (a) The concentration of NO 5.3 μm observed by SABER in the altitude range between 65° S and 75° S, (b) The electron flux with energies >30 keV observed by MIPED and 3-hour average Ap index, (c) The concentration of NO observed by Microwave radiometer, (d) The electron flux with energies >300 keV observed by MIPED and 3-hour average Ap index [*Newnham et al.*, 2011].

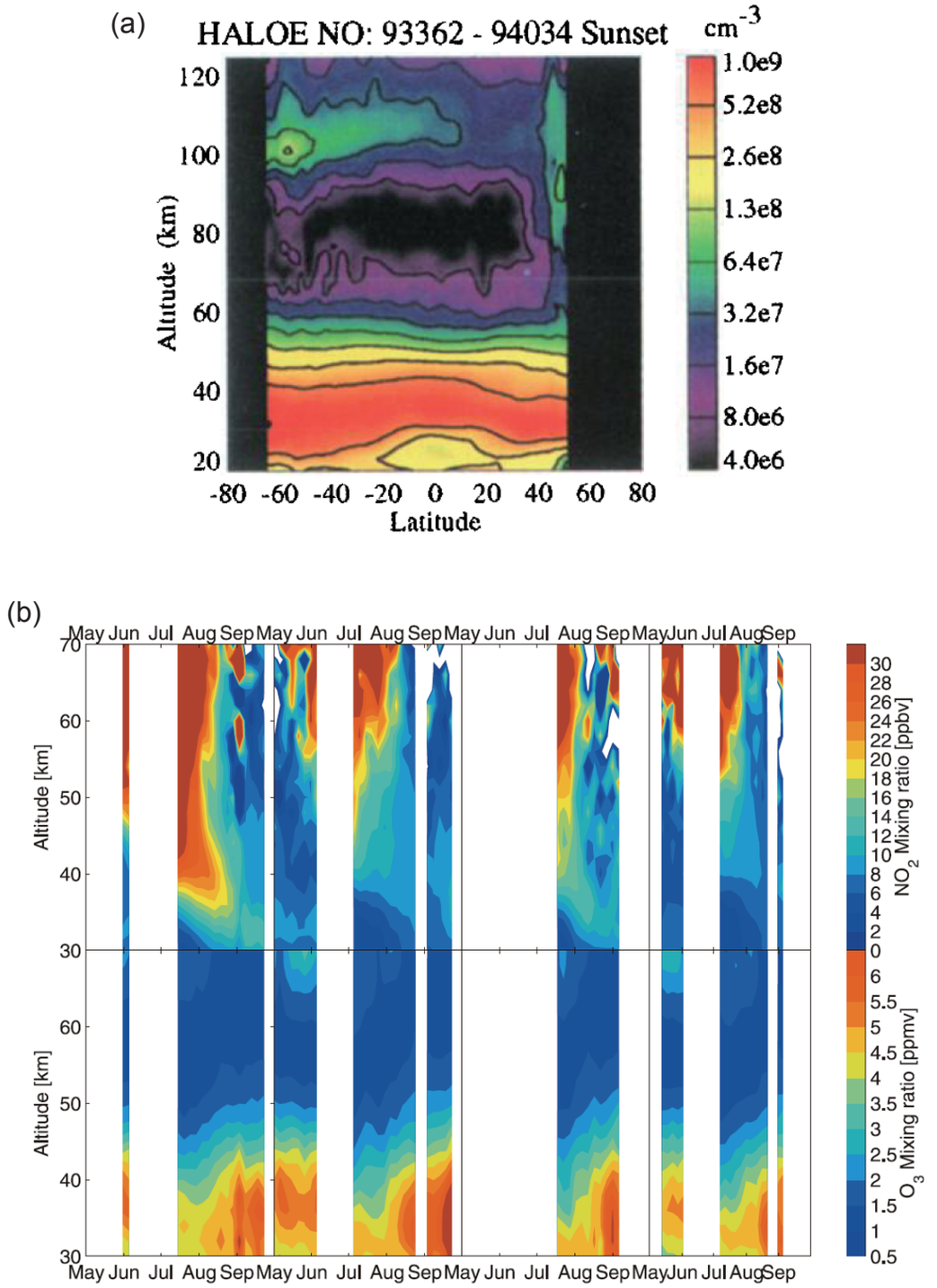

Figure 1.6 (a) The NO densities between 20 km and 120 km observed by HALOE. The NO densities are daily zonal means from December 28, 1993 to Feb 3, 1994. [*Siskind and Russell III.*, 1996]. (b) (Top) The NO_2 mixing ratio observed by GOMOS in the southern hemisphere polar winter (months May-Sep). (Bottom) Same as top but for ozone [*Seppälä et al.*, 2007].

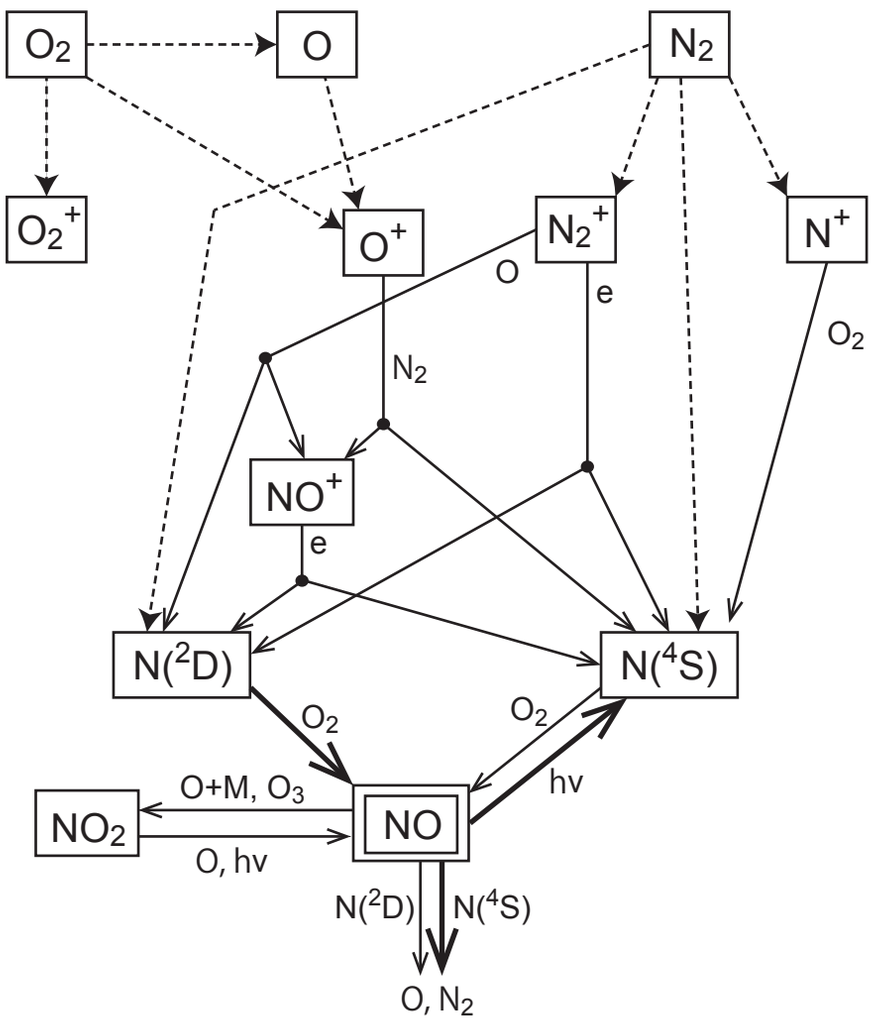

Figure 1.7 Chemistry of nitrogen compounds in the mesosphere and thermosphere. Dashed lines indicate the primary interaction due to EPP. Solid lines indicate neutral and ion-neutral reactions, although we omit the ion-neutral reactions which do not directly relate production of atomic nitrogen (right column of Table 1.1).

Chapter 2

Instruments and Observation

2.1 Syowa Station in Antarctica

The observation site is Syowa Station (69.00°S, 39.85°E, Λ=66°, 29m alt.) in Antarctica. Syowa Station is located on East Onglu Island 4 km to the west of the eastern coast of Lutzow-Holm Bay, Antarctica as shown in Figure 2.1 and 2.2. The meteorological average year values between 1981 and 2010 at Syowa Station observed by Japan Meteorological Agency: the Surface pressure is 984 hPa, the relative humidity is 67 %, the monthly-averaged maximum air temperature is -0.7 degree Celsius in January, the monthly-averaged minimum air temperature is -19.4 degree Celsius in September, the wind speed is 6.7 m/s (Northeast wind), the number of snow days is 200 days, and the hours of sunlight are 1926 hours. In 2012 and 2013, the numbers of snow days were 226 and 191, respectively, and the hours of sunlight were 1848 and 1860, respectively. At Syowa Station, the polar night is continuous for 43 days from the end of May to the beginning of July. During the summer, daylight is continuous for 60 days from the end of November

to the middle of January.

2.2 Millimeter-wave spectroscopic radiometer

Our observation system which is millimeter-wave spectroscopic radiometer is located in the optical observation building at Syowa Station as shown in Figure 2.3. The observation windows which are facing south and the zenith are made of polystyrene which completely transmit a millimeter-wave radiation. Figure 2.3 also shows the millimeter-wave spectroscopic radiometer. It was assembled between December 2010 and February 2011 by the 52nd Japanese Antarctic Research Expedition. Since March 2011, we have carried out observations by using a millimeter-wave spectroscopic radiometer.

Figure 2.4 is a block diagram of the millimeter-wave spectroscopic radiometer. The radiometer consists of a quasi-optical system, a heterodyne receiver system, and a digital fast Fourier transform (FFT) spectrometer. The details of each component are described below.

The quasi-optical system (Figure 2.5) consists of a flat rotating mirror, a paraboloidal mirror, two ellipsoidal mirrors, and a path length modulator (PLM). We used offset–Gregorian telescope optics. The flat rotating mirror switches the direction of incoming signals between the sky and reference sources. The paraboloidal mirror collects millimeter-wavelength radiation. Its diameter of 12 cm is sufficient to produce a beam width or a beam divergence of 1.0° full-width-at-half-maximum (FWHM) at a frequency of 250 GHz. The two ellipsoidal mirrors guide millimeter-wavelength radiation to a heterodyne receiver system. The PLM is located in the middle of the beam waist between the

paraboloidal and first ellipsoidal mirror. The PLM continually and periodically changes the length of the light path by half a wavelength by means of a reciprocating motion of a rooftop mirror to reduce the standing waves that cause artificial spectral baseline ripple [*Gustincic*, 1977; *Mizuno et al.*, 2002]. Figure 2.6 shows the beam size profiles along with the distance from horn. We find that the PLM locate in the middle of the beam waist. Measured values (phase-H and phase-E) show within 10% and 20% of designed values, respectively, and these are the permissible margin of mirrors.

The receiver system uses a heterodyne technique in which a nonlinear electronic device called a "mixer" changes the frequency of the original millimeter-wavelength signal to a much lower frequency by combining another frequency signal from an oscillator called a "local oscillator" (LO). The receiver system consists of a feed horn, a Superconductor-Insulator-Superconductor (SIS) mixer [see, for example, *Tucker and Feldman*, 1985, for more details], a high-electron-mobility transistor (HEMT) amplifier, and a room-temperature, intermediate frequency (IF) circuit (Figure 2.7). With the feed horn, a quasi-optical mode signal collected by the mirrors is transformed to a waveguide mode suitable for the following mixer receiver. A corrugated conical horn is used in the present system. The SIS mixer and HEMT amplifier are enclosed in a vacuum chamber, where they are cryogenically cooled down to ~4 K and ~12 K, respectively, by a closed-cycle helium mechanical refrigerator. The SIS mixer junction was fabricated in the clean room of the National Astronomical Observatory of Japan by Nagoya University staff members. The mixer operates in a double side-band (DSB) mode, and the receiver system noise temperature is 70 K. The LO signal is generated by amplifying the continuous wave (CW) signal from a synthesized signal generator by a factor of 18 with a ×6 active multiplier

and a frequency tripler. The IF of the output signal of the SIS mixer is ~6 GHz. For observations of the NO emission at 250.796 GHz, the LO frequency was tuned to 244.746 GHz. This IF signal of the SIS mixer is amplified and down converted by the concatenated second and third mixers and amplifiers in the room-temperature IF circuit, and the final output signal is adjusted for the specification of the digital FFT spectrometer.

The spectrometer is an Acqiris Digital FFT Spectrometer (DFS), model AC240, manufactured by Agilent Technologies. Its fast A/D sampling rate of 2×10^9 samples/s provides wide-frequency coverage of spectroscopy at 1 GHz with Nyquist sampling and 16,383-channel FFT data. Spectral data in the frequency domain are obtained from 32,768 points of 8-bit A/D data in the time domain. The time to acquire these data is 16.4×10^{-6} s. For the observations described here, we used a Hanning window apodization and obtained the spectrum with a resolution of 61 kHz.

2.3 Observation method

At a frequency ν, the output power of the spectrometer, $P_{sky}(\nu)$, includes the contribution of tropospheric thermal emissions and the system noise of the observing system as well as the contribution from the objective molecular line emission, as expressed in Equation (2.1). It was necessary to eliminate the superfluous term to obtain the final molecular spectra, $T_{NO}(\nu)$. The output power when the observing beam is pointed toward the zenith is

$$P_{\mathrm{sky}}(\nu) = \alpha(\nu)\left\{T_{\mathrm{NO}}(\nu)\cdot\exp\left(-\tau(\nu)\right) + T_{\mathrm{sky}}(\nu)\left(1-\exp\left(-\tau(\nu)\right)\right) + T_{\mathrm{sys}}(\nu)\right\} \quad (2.1)$$

where T represents the equivalent brightness temperature, which is proportional to the intensity, because the Rayleigh-Jeans approximation is adequate in the millimeter wavelength range and within the range of typical atmospheric temperatures; τ is the optical depth of the tropospheric absorbing layer; and α is the conversion coefficient between radiation power and the output voltage of the spectrometer.

We used a frequency switching technique [*Nagahama et al.*, 1999] to eliminate the background continuum of the spectrum, i.e., the second and third terms of equation (2.1). In this switching technique, the LO frequency is shifted by an amount $\Delta\nu$ between the "on" and "off" conditions. In the NO observations reported here, we shifted the frequency by 100 MHz every 2 s at the second LO frequency. Because the frequency shift of 100 MHz was larger than the expected line width of NO above the upper stratosphere, the spectral intensity [i.e., the first term of equation (2.1)] became almost zero for the "off" data. However, the values of τ, T_{sky}, and T_{sys} were not very sensitive to the frequency, and those values were almost the same for both the "on" and "off" data. The second and third terms of equation (2.1) were therefore the same for both the "on" and "off" data. We could therefore eliminate the background continuum by subtracting the frequency-shifted "off" data from the "on" data.

To extract the spectral data, $T_{\mathrm{NO}}(\nu)$, from the post-switching data, it was necessary to determine the conversion coefficient, α, and the optical depth, τ. The value of α was determined by a calibration measurement of hot- and cold-load references. The output powers of the hot and cold references are expressed as

follows:

$$P_{\mathrm{hot}} = \alpha\{T_{\mathrm{hot}} + T_{\mathrm{sys}}\} \tag{2.2}$$

$$P_{\mathrm{cold}} = \alpha\{T_{\mathrm{cold}} + T_{\mathrm{sys}}\} \tag{2.3}$$

where T_{hot} and T_{cold} are radiation temperatures of 300 K and 77 K, respectively, because the materials of the hot- and cold-loads were considered to be black bodies, and both the radiation temperature and the physical temperature are identical at millimeter-wave length. The conversion coefficient was obtained from equations (2.2) and (2.3) as follows:

$$\alpha = \frac{I_{\mathrm{hot}} - I_{\mathrm{cold}}}{T_{\mathrm{hot}} - T_{\mathrm{cold}}} \tag{2.4}$$

The optical depth of the tropospheric absorbing layer, τ, was measured by a "sky tipping" method [*Ulich et al.,* 1980] every 13 minutes.

Compared with other switching techniques such as elevation angle switching [e.g., *Parrish et al.*, 1988; *Maier et al.*, 2001] and load switching, frequency switching has some advantages and disadvantages. One of the important advantages is that, during frequency switching, the "off" data provide spectral information about the objective molecular line at the shifted spectrometer channel. By using this information, the signal-to-noise ratio is improved by a factor of $\sqrt{2}$. However, frequency switching is no longer adequate for broad line emissions whose line widths are broader than the frequency shift. Thus, the frequency switching technique is not suitable for molecules distributed mainly below the middle stratosphere.

2.4 Observation schedule

Since March 2011, we have carried out observations by using a millimeter-wave spectroscopic radiometer. We observed the spectral line of ozone at 235.709 GHz and NO_2 at 247.355 GHz until December 2012. Since January 2012, we have carried out observations of the spectral lines of ozone at 239.093 GHz and of NO at 250.796 GHz. In this paper, we report the results of the NO observations during 2012–2013.

We have observed the NO lines continuously during the day, except for ozone observation times, for one hour four times each day since January 2012. Observations could be made with the millimeter-wave spectroscopic radiometer during the day. However, the NO and ozone emissions were attenuated by 5–40% if the observation window was covered with snow or ice. The amplitude of the attenuation fluctuated from hour to hour, depending on the weather conditions, and such fluctuations compromised the accuracy of the data. We therefore suspended the measurements when the observation window was covered with snow or ice.

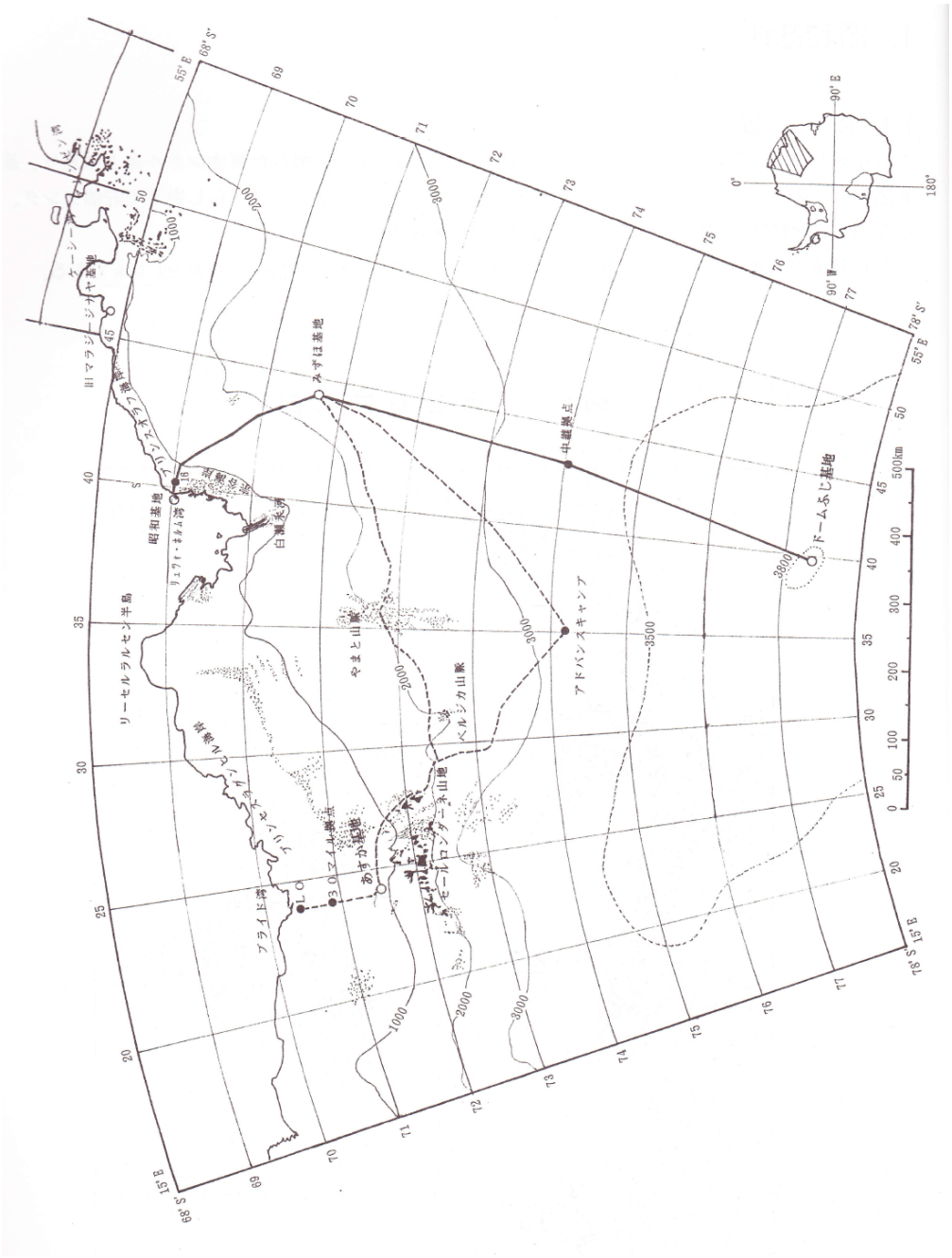

Figure 2.1 The map of the Northeast area in Antarctica (NIPR, 2010)

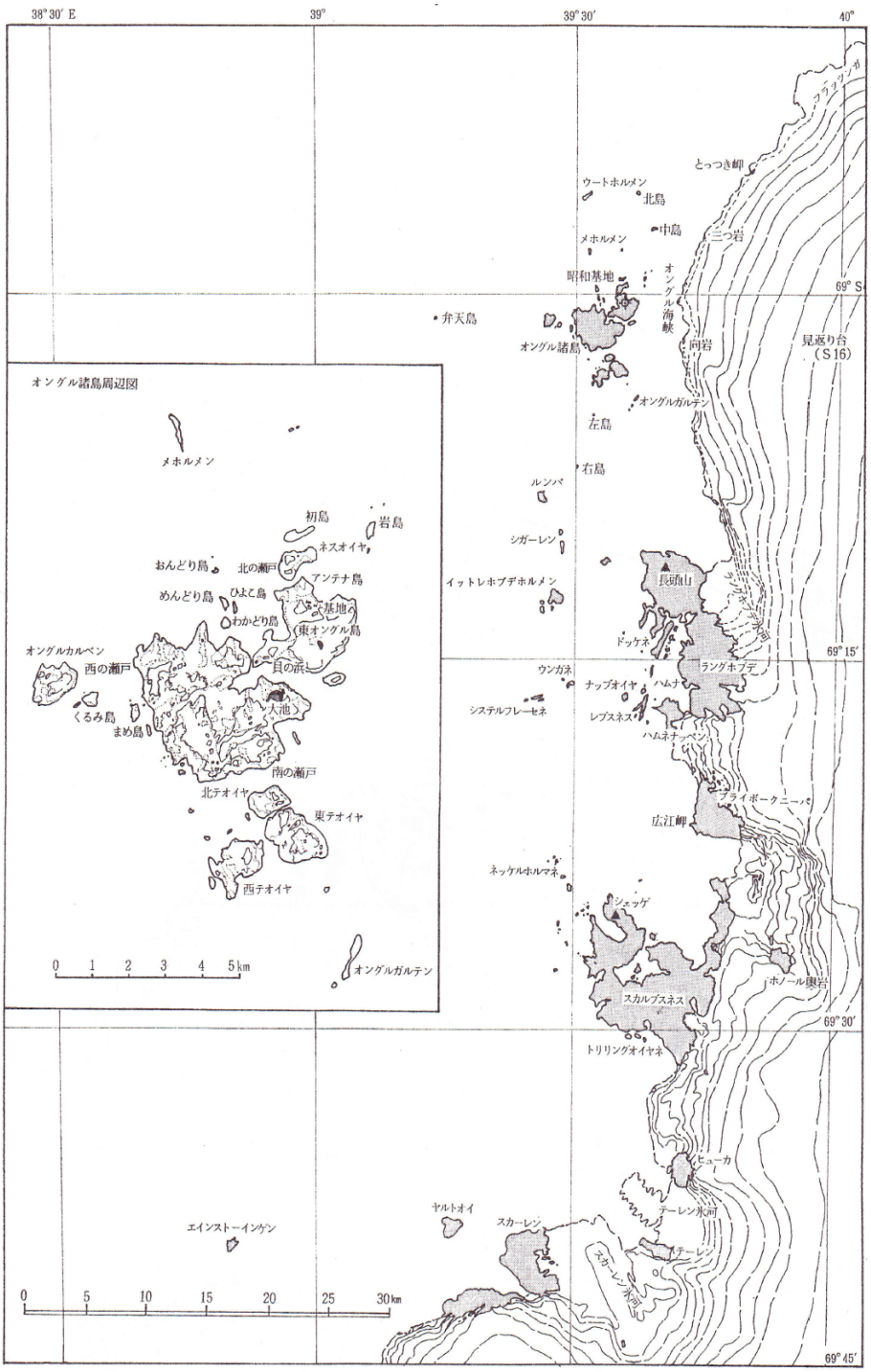

Figure 2.2 The map of the Syowa station area in Antarctica (NIPR, 2010)

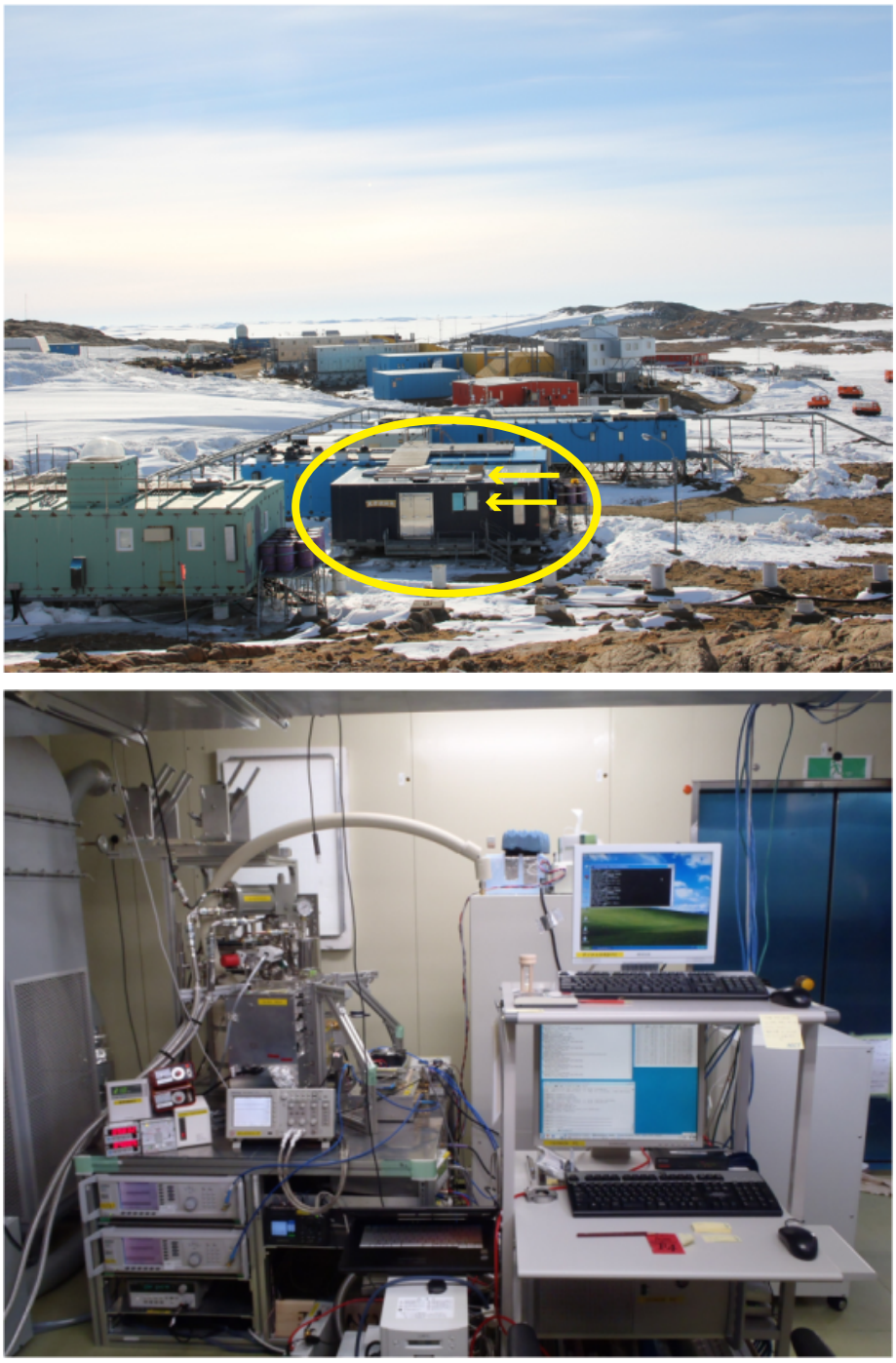

Figure 2.3 (top) The main area of the Syowa station. A yellow circle indicates the optical observation building and yellow narrows indicate the observation windows which are facing south and the zenith are made of polystyrene. (bottom) The millimeter-wave spectroscopic radiometer in the optical observation building.

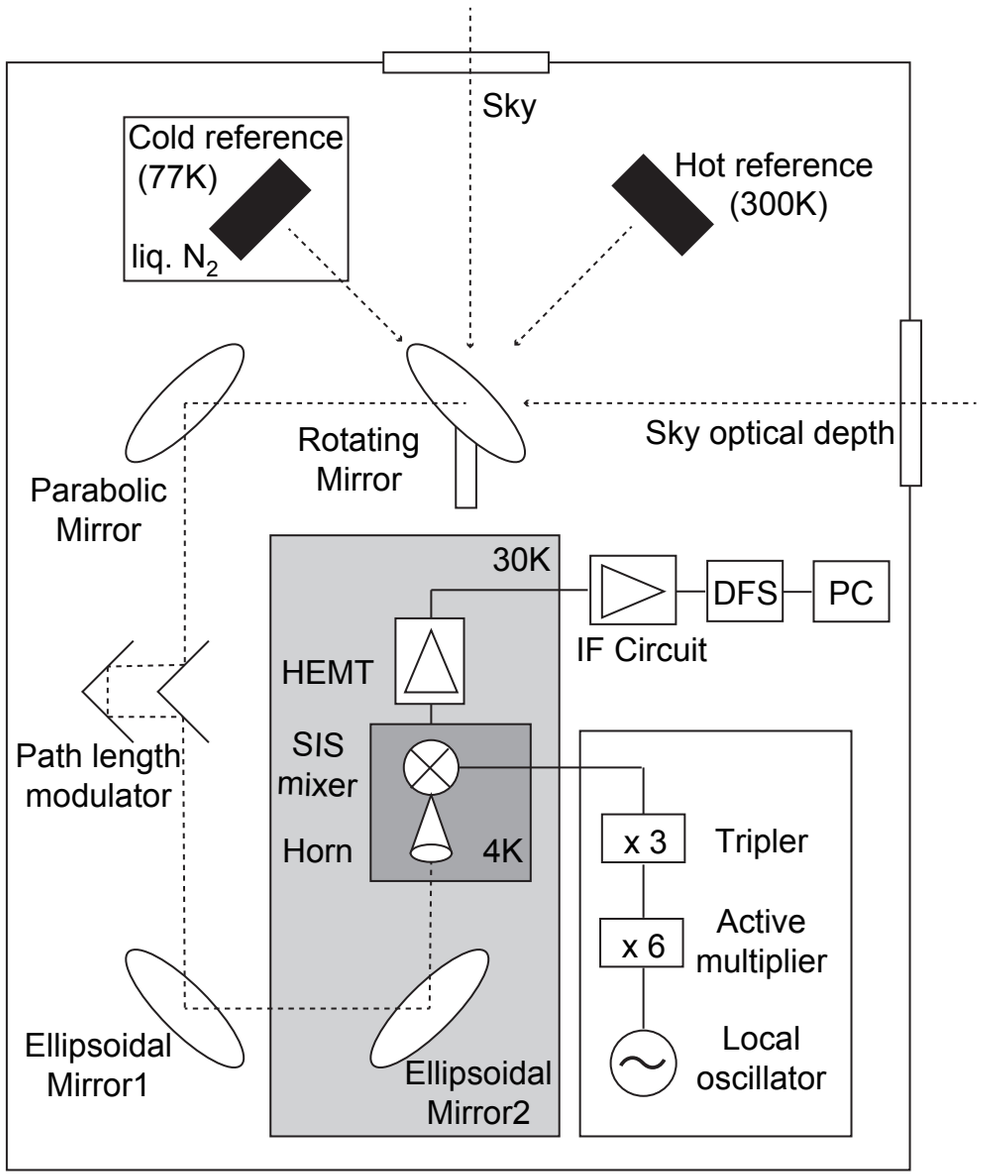

Figure 2.4 Block diagram of the ground-based millimeter-wave spectroscopic radiometer at Syowa Station. Dotted lines show optical paths. The gray box schematically indicates a vacuum chamber in which the radiometer components are cryogenically cooled down to ~4 K by a closed-cycle, helium, mechanical refrigerator. At the reference cold load, a radio-wave absorber is put into liquid N2 at a temperature of 77 K.

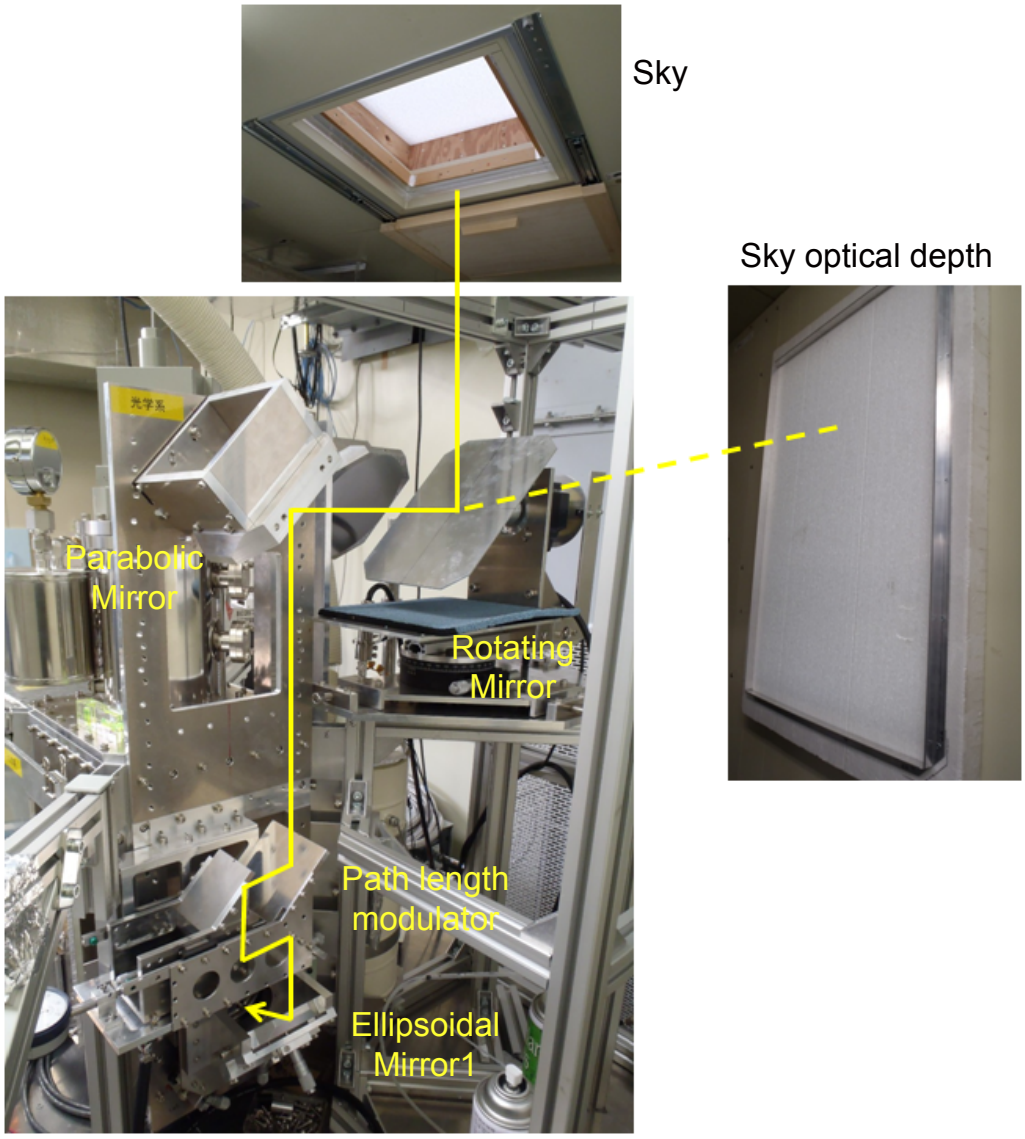

Figure 2.5 The quasi-optical system. It consists of a flat rotating mirror, a paraboloidal mirror, two ellipsoidal mirrors and a path length modulator (PLM). Yellow lines show an optical path.

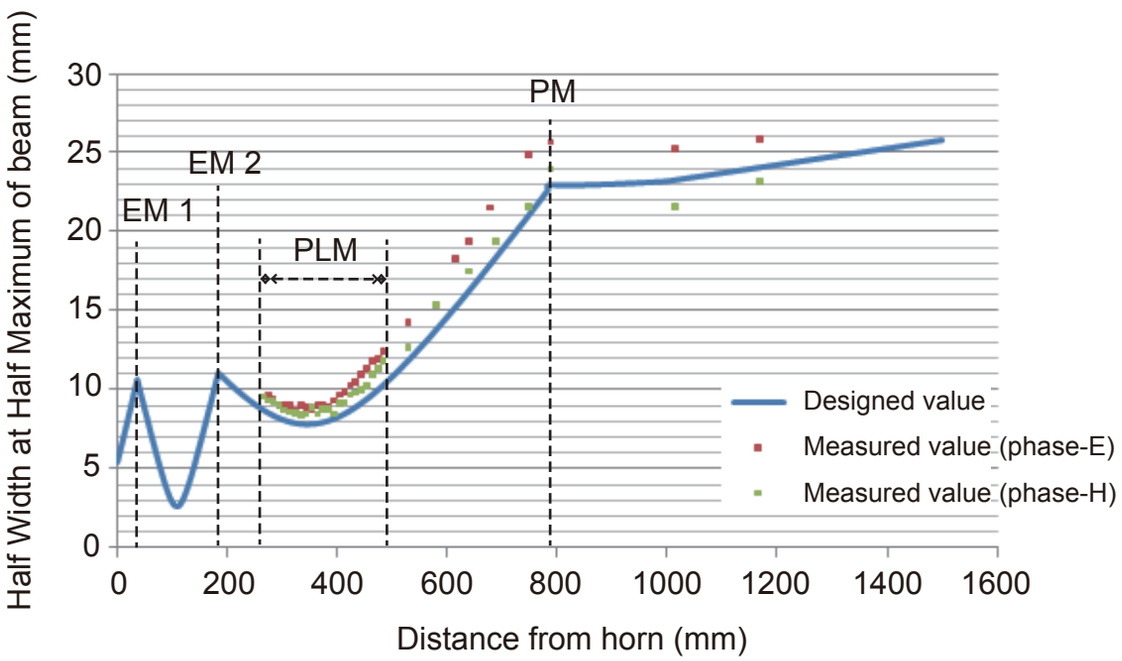

Figure 2.6 The beam size profiles along with the distance from horn. Blue curve indicates the designed value, and red and green squares indicate the measured value in phase-E and phase-H, respectively. Black dashed lines indicate the position of optical components. EMs are Ellipsoidal Mirrors, PLM is Path length modulator, PM is Paraboloidal Mirror.

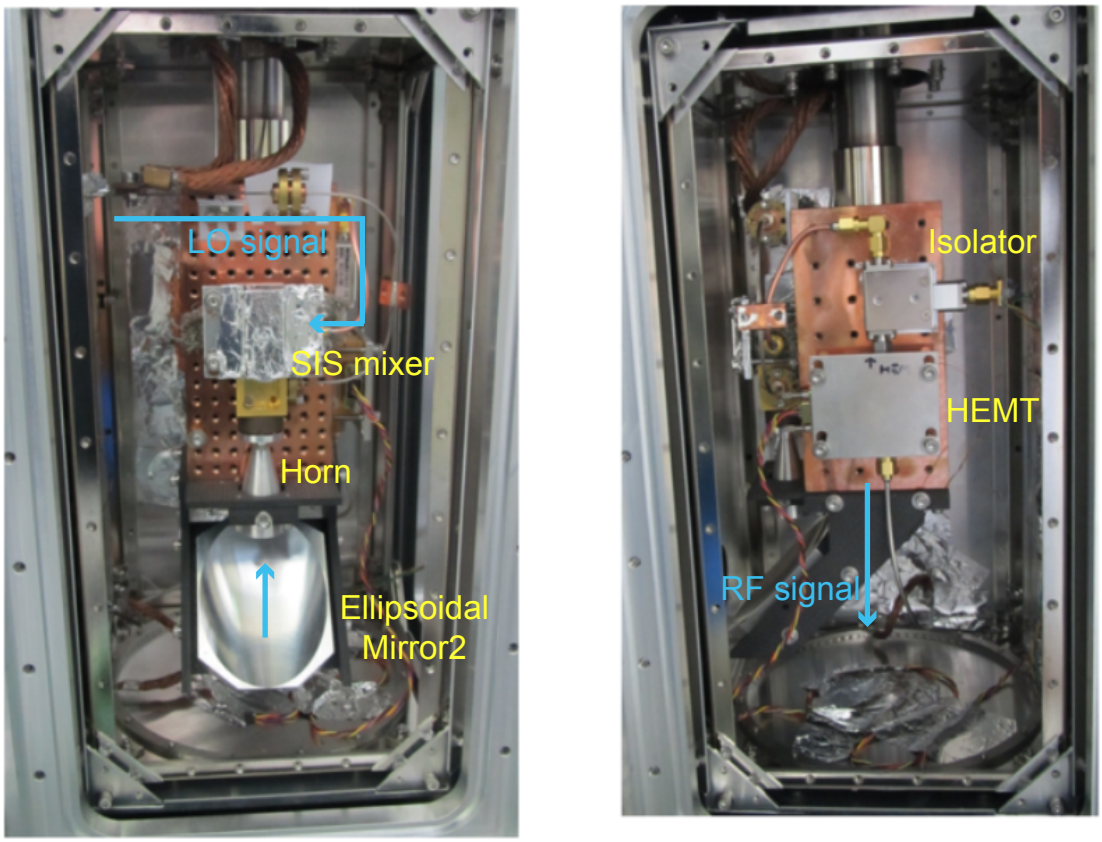

Figure 2.7 The inside of the dewar. SIS mixer and HEMT are hidden their jigs. A block made of oxygen free copper and the inside of the dewar shield keep the temperature at 4 K and 30 K, respectively. Blue lines indicate LO and RF signal line.

Chapter 3

Data analysis

3.1 Details of NO spectrum

Figure 3.1 shows the 1-day-averaged spectrum of NO emission at 250.796 GHz on 11 July 2012. This spectrum had the best signal-to-noise ratio during the observation period. The root mean square (rms) noise was 17 mK. The rms noise depends on the total observation time and the optical depth. The optical depth, which depends on the concentration of water vapor in the troposphere, fluctuated with the seasons and with daily weather. The average optical depths in the summer and winter were 0.3 and 0.1, respectively, and, especially after polar night, they were smaller than 0.1 at Syowa Station. We therefore had good conditions for observing millimeter-wave emissions during the winter. Throughout the observation period, the lowest rms noise was 13 mK on 27 September 2012, and the average rms noise was 20 mK.

Figure 3.1 shows the spectrum after baseline smoothing, performed by subtracting a cubic polynomial fitted to the data from 250.781 to 250.811 GHz.

Through this baseline smoothing, any broad line component, such as the emission from tropospheric NO, was removed from the spectrum. Figure 3.2 illustrates the baseline smoothing procedure for the spectrum shown in Figure 3.1. When we smoothed the baseline, we removed the NO emission from 250.7954 to 250.7974 GHz.

During the two-year observation period, we selected daily-averaged spectral data that satisfied the requirement that the rms noise be less than 40 mK and the optical depth be less than 0.33. Using these criteria, we obtained 197 and 172 daily NO spectra in 2012 and 2013 [until 30 September; day of year (DOY) 273], respectively. Most daily NO spectra were similar to the spectrum on 11 July 2012 shown in Figure 3.1. We needed to fit a cubic polynomial for each spectrum because the baseline differed in each profile.

3.2 Estimation of NO emitting region

The most remarkable feature of the results is that the line widths of the spectra were narrow. Figure 3.3 shows the 1-day-averaged spectrum of NO on 29 April 2012 (DOY 120). The rms noise in this case was only 16 mK because the observation time was relatively long (76% of 24 h) and the optical depth was good, about 0.12–0.18. On this day, 17% of the 24 h was used for ozone observations. The NO spectrum was fitted equally well by single Gaussian and single Lorentzian curves. The rms values of the fitting residuals were 13 mK and 14 mK for the Gaussian and Lorentzian curves, respectively. The FWHM of the line width was 0.5 MHz in both cases. Throughout the observation period, most of the daily NO spectra had similarly narrow line widths.

The actual line shape is a convolution of a Gaussian and a Lorentzian, i.e. a so-called Voigt function. The Gaussian and Lorentzian components correspond to thermal broadening and pressure broadening, respectively [*Janssen*, 1993]. Below 65 km the Lorentzian component becomes significant, and it is possible to retrieve the vertical profile of the NO concentration by using the pressure broadening relationship. In the present case, it was difficult to obtain vertical profiles from the spectra because they had narrow line widths that were fitted by Gaussian functions. The implication is that the region responsible for the NO emission spectrum was above 65 km. Below ~75 km, NO is expected to show diurnal variation; NO decreases during the night when it reacts with O_3 to form NO_2, and it increases during the day as a result of photo-dissociation of NO_2, which forms NO. Because we did not see such a diurnal variation, we assumed the altitude associated with most NO production and consumption to be above 75 km. An upper limit on the emitting region can be estimated from the kinetic temperature derived from the Doppler broadening line width. The observed line width of 0.5 MHz corresponds to 220–230 K. In the lower thermosphere, the temperature abruptly rises with increasing altitude. By comparing the temperature calculated with the MSIS-E-90 model above the location of Syowa Station, we concluded that ~105 km was an appropriate value for the upper limit. From the line shapes, we estimated that the region of NO emissions was in the altitude range 75–105 km.

3.3 Derivation of the column density of NO

We analyzed each spectrum and obtained the column density because we could not retrieve the vertical profile by using the pressure-broadening relationship. First, we obtained the daily averaged spectrum and clipped out the central 30 MHz, from 250.781 to 250.811 GHz. Second, we smoothed the baseline of the spectrum by subtracting a fitted cubic polynomial (e.g., Figure 3.2). Finally, we calculated the column density of NO from the integrated intensity of the brightness temperature of the daily average spectrum.

We derive the relationship between the column density and the spectral line intensity based on the equations in Chapter 2 of *Janssen et al.* [1993]. If molecules are distributed above a lower altitude limit, h_0, the observed brightness temperature toward the zenith is written as

$$T_{\mathrm{b}}^{*}(\nu) = \int_{h_0}^{\infty} T(h)\alpha(\nu,h)\,\mathrm{e}^{-\tau(\nu,h)}\mathrm{d}h \tag{3.1}$$

where $T(h)$ is the atmospheric temperature at an altitude of h, $\alpha(\nu,h)$ is the absorption coefficient, and $\tau(\nu,h)$ is the optical depth between h_0 and h, i.e., $\mathrm{e}^{-\tau(\nu,h)}$ is the transmittance of the layer between h and h_0. If the spectral line is optically thin, equation (3.1) can be written as

$$T_{\mathrm{b}}^{*}(\nu) \sim \int_{h_0}^{\infty} T(h)\alpha(\nu,h)\,\mathrm{d}h \tag{3.2}$$

The absorption coefficient, $\alpha(\nu)$, is expressed by using molecular parameters as

$$\alpha(\nu) = n\, S_{\mathrm{fi}}(T)\mathrm{F}(\nu, \nu_{\mathrm{fi}}) \tag{3.3}$$

where n is the number density of the objective molecule, S_{fi} is the line intensity of the transition from the i-state to the f-state of a molecule at a temperature T, and $F(\nu, \nu_{\mathrm{fi}})$ is the line shape function. Then equation (3.2) is written as

$$T_{\mathrm{b}}^{*}(\nu) \sim \int_{h_0}^{\infty} nT(h)\, S_{\mathrm{fi}}(T) F(\nu, \nu_{\mathrm{fi}})\, \mathrm{d}h \tag{3.4}$$

If we assume local thermodynamic equilibrium and in the case $\nu_{\mathrm{fi}}(\mathrm{GHz}) < 10T(\mathrm{Kelvin})$, $\mathrm{S_{fi}}$ can be approximately written as

$$S_{\mathrm{fi}}(T) = S_{\mathrm{fi}}(T_0)\frac{T_0 Q(T_0)}{TQ(T)}\exp\left[\frac{E_{\mathrm{f}} + E_{\mathrm{i}}}{2\mathrm{k}T_0}\left(1 - \frac{T_0}{T}\right)\right] \tag{3.5}$$

where $Q(T)$ is the internal partition function, E_{i} and E_{f} are the energy level of the initial and final states, respectively, k is the Boltzmann constant, and T_0 is a specified temperature. For linear molecules, the temperature dependence of $Q(T)$ is approximated as

$$\frac{Q(T_0)}{Q(T)} = \frac{T_0}{T} \tag{3.6}$$

We assumed the following conditions for our calculations: first, the NO-emitting region was optically thin; second, the temperature was uniform at 300 K in the column of NO; and third, the majority of the line was emitted within

±1 MHz, i.e.,

$$\int_{\nu_0-1\ \mathrm{MHz}}^{\nu_0+1\ \mathrm{MHz}} F(\nu,\nu_{\mathrm{fi}})\mathrm{d}\nu \sim 1 \tag{3.7}$$

Then, integration of equation (3.4) over the ±1 MHz interval gives

$$\int_{\nu_0-1\ \mathrm{MHz}}^{\nu_0+1\ \mathrm{MHz}} T_{\mathrm{b}}^{*}(\nu)\,\mathrm{d}\nu \sim \int_{\nu_0-1\ \mathrm{MHz}}^{\nu_0+1\ \mathrm{MHz}} \int_{h_0}^{\infty} n\,S(T)F(\nu,\nu_{\mathrm{fi}})T(h)\,\mathrm{d}h\mathrm{d}\nu \tag{3.8}$$

$$= \int_{h_0}^{\infty} n\ \mathrm{d}h \cdot \frac{T_0^2}{T} S(T_0) \int_{\nu_0-1\ \mathrm{MHz}}^{\nu_0+1\ \mathrm{MHz}} F(\nu,\nu_{\mathrm{fi}})\mathrm{d}\nu \tag{3.9}$$

$$= N_{\mathrm{NO}} \cdot \frac{T_0^2}{T} S(T_0) \tag{3.10}$$

where N_{NO} is the column density of NO. To derive equation (3.9), we used the fact that the exponential term in equation (3.5) can be set to unity for T_0 = 300 (K).

The left-hand side of equation (3.10) is the integrated intensity. We assumed the channel bandwidth of dynamic frequency selection to be 6.1039 × 10^{-2} MHz. We took the $S(T_0)$ of NO emission at 250.796 GHz from the Jet Propulsion Laboratory catalog (http://spec.jpl.nasa.gov/ftp/pub/catalog/catform.html) [*Pickett et al.*, 1998]. The equation for $S(T_0)$ is then $S(T_0) = 10^{-4.5553}$ (nm^2 MHz) at T_0 = 300 (K). The relationship between the integrated intensity and the NO column density is then given by

$$N_{\mathrm{NO}}\ [\mathrm{cm}^{-2}] = 3.9 \times 10^{13} \times T_{atm} \times \int_{\nu_{min}}^{\nu_{max}} T_b\,\mathrm{d}\nu \quad [\mathrm{K}^2\ \mathrm{MHz}] \tag{3.11}$$

where T_{atm}, T_b are atmospheric temperature and brightness temperature of the spectral line at each frequency.

The uncertainty of the column density of NO calculated with equation (3.11) is directly proportional to the uncertainty of the column average of the atmospheric temperature, T_{atm}. In this study, we assumed a constant atmospheric temperature of 200 K for the column density estimation. Application of the MSIS-E-90 atmospheric model (http://omniweb.gsfc.nasa.gov/vitmo/msis_vitmo.html) to the location of Syowa station indicates that the average temperature between ~75 and ~105 km changes from ~180 K to ~215 K. At ~90 km, the temperature decreases to ~140 K in the polar summer, but for more than 150 days in the winter the temperature is almost ~200 K. In contrast, at ~105 km, the temperature increases to ~260 K during the polar summer, but for more than 150 days in the winter the temperature is almost ~200 K. Because we were unable to derive the vertical distribution of NO from the spectral line data, there must be an error due to the assumed distribution of temperature. Because the column density is proportional to the temperature, there is an average error of ~±10% and the maximum error may become ~±30% during the summer.

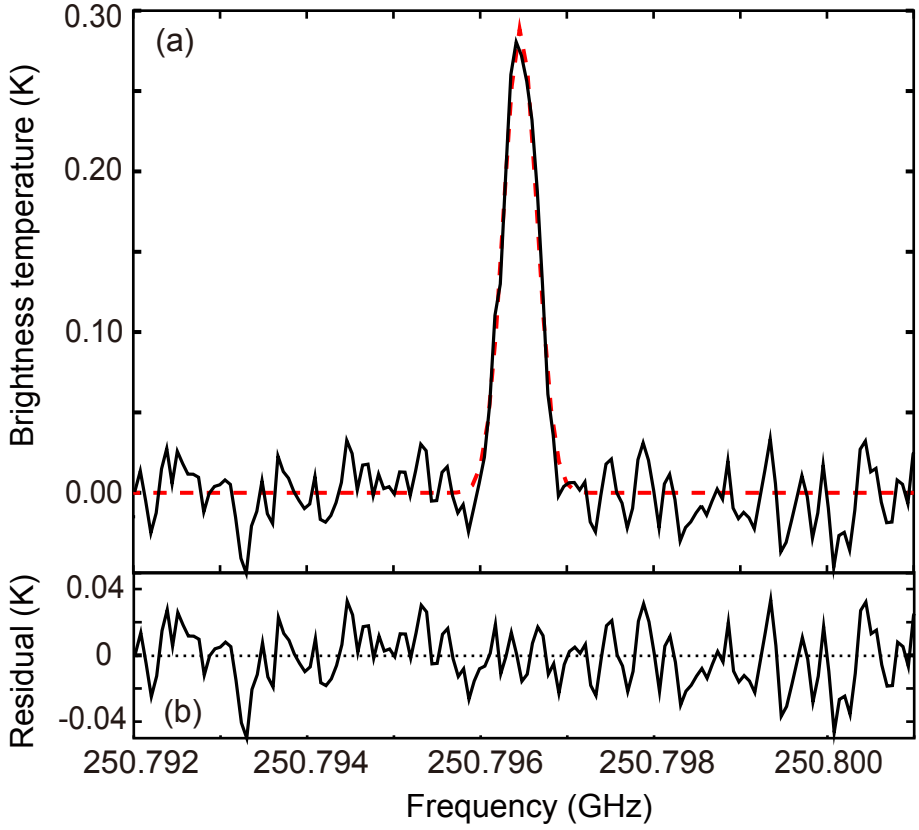

Figure 3.1 (a) Spectrum of nitric oxide at 250.796 GHz on 11 July 2012 (DOY 193). The red dotted curve shows a fitted Gaussian line shape function that has a full width at half maximum (FWHM) of 0.5 MHz. (b) Residual spectrum, in which the Gaussian fit has been subtracted.

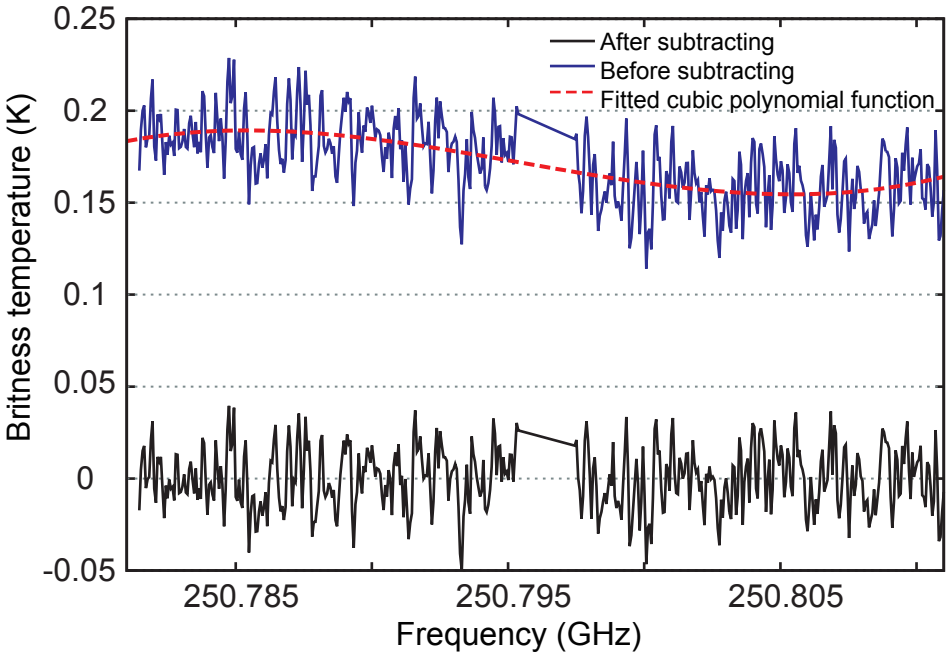

Figure 3.2 The baseline profile of the NO spectra on 11 July 2012. Blue and black lines indicate the spectrum of the NO before and after subtraction, respectively, of the cubic polynomial function, which is indicated by the red dashed line.

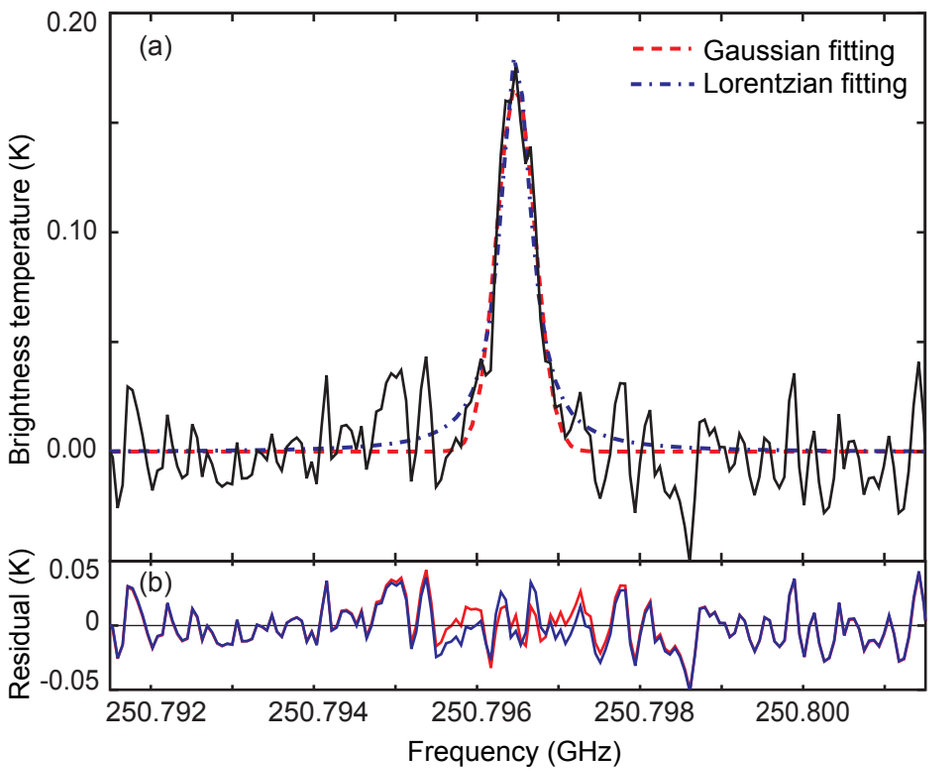

Figure 3.3 (a) Spectrum of nitric oxide at 250.796 GHz on 29 April 2012 (DOY 120). The red dashed curve shows a fitted Gaussian line shape function that has a FWHM of 0.55 MHz, and the blue dash-dotted curve is a fitted Lorentzian line shape function. (b) Residuals for the fitting by Gaussian and Lorentzian functions in red and blue, respectively.

Chapter 4

Temporal Variations of Nitric oxide in 2012-2013

In this chapter, we report results of NO observations between January 2012 and September 2013. In Section 4.1, we report the results and discuss the seasonal variations of NO concentrations. We found a clear seasonal cycle, with a peak in winter and a trough in summer. In section 4.2, we report our results and discuss variations of NO in a timeframe of several days. We compare the column density of NO, after subtraction of seasonal variations, with the fluxes of energetic protons and electrons observed by the Geostationary Operational Environmental Satellite (GOES) and Polar Orbiting Environmental Satellite/Meteorological Operational (POES/METOP) satellites.

4.1 Long-term variation of NO

4.1.1 Data analysis

Figure 4.1 shows the time series of the daily average NO column density in the altitude range 75–105 km. The most remarkable feature was a clear seasonal variation; the NO column density increased in winter and decreased in summer, and the annual patterns were very similar in 2012 and 2013. We calculated 31-day running averages of the NO column density to smooth out the short-term fluctuations (discussed in section 4.2). Also, we used annual and semi-annual sinusoidal functions to fit the time series of NO column densities to elucidate the periodicity of the seasonal variation. The fitting function was

$$\mathrm{f(x)} = 0.4\sin\frac{2\pi}{365}(x-74) - 0.2\sin\frac{4\pi}{365}(x-36) + 0.6 \qquad (4.1)$$

Both the smoothed and fitted curves are shown in Figure 4.2a. These two curves were in good agreement and lay within the typical error bars of the NO column densities. The standard deviation of anomaly from the sinusoidal fitting equation (4.1) is 0.29, and hereafter we call it as the seasonal fitting error. However, the actual fitting error is regarded smaller than this value because the data include short-term variations to be disccued in the next chapter. The apparent seasonal variation was periodic, the suggestion being that the pattern of variation was related to climatological phenomena rather than to solar activity.

To inform discussion of the possible causes of the seasonal variation, we show the vertical profiles of CO in Figure 4.2b and the eastward wind velocity around 70-84 km altitude in Figure 4.2c. These are proxies related to the possible contribution of atmospheric circulation to the transport of NO produced in the upper region; CO is a good tracer of atmospheric vertical transport because of its long chemical lifetime, and the change in wind direction from westward to eastward is an indication of when downwelling begins, that is, when polar vortex activity starts. The CO vertical profile was recorded by the Microwave Limb Sounder (MLS) onboard the Earth Observing System (EOS) Aura satellite [*Schoeberl et al.,* 2006]. We used Level 2 CO data (Version 3.3) [*Livesey et al.,* 2006, 2011]. We calculated daily CO vertical profiles with data from latitudes between –65° and –75°, longitudes between –180° and 180°, and pressures between 0.1 hPa and 0.01 hPa. The wind velocity data were obtained by the MF radar at Syowa Station [*Tsutsumi et al.,* 2001].

In addition, in order to evaluate the photochemical effect, we have superimposed the yearly variation of the daylight hours at 100 km in Figure 4.2a. The number of daylight hours was longer at an altitude of 100 km than at ground level, and was about 7 hours even during the polar night.

4.1.2 Discussion

There are several possible causes of the seasonal variation. Because the period of high NO column density is almost coincident with the period of the polar vortex, atmospheric descent of the polar vortex is one possible cause of the

seasonal variation. For example, on the basis of satellite observations, *Randall et al.* [2001, 2007] and *Seppälä et al.* [2007] suggested that the descent of the polar vortex combined with the impact of the EPP, which increases the NO_x concentration in the thermosphere, causes the enhancement of NO_x in the middle atmosphere. Photochemistry is another possible cause, because the photoperiod is drastically different between summer and winter in the polar regions.

First, we consider the possibility that the seasonal variation of NO was related to the descent of the polar vortex. As shown in Figure 4.2a and 4.2b, the column density of NO began to grow at the end of March, and CO began to descend at the same time. The eastward wind speed became positive around the end of March as shown in Figure 4.2c. From the CO vertical profile and eastward wind velocity, we conclude that atmospheric circulation shifted to a winter mode in the southern hemisphere at that time. It seems that NO-rich air descended from the lower thermosphere into our observation region, which was in the altitude range 75–105 km.

In contrast, the NO column density and the CO profile behaved differently while they were decreasing in the late winter and early spring. The CO concentration remained above 5 ppmv at altitudes above 75 km until the end of October, and the eastward wind speed remained positive until the end of September. We conclude that lower thermospheric air was still descending into the mesosphere in September, whereas the column density of NO began to decrease after the beginning of the polar night in the middle of July. Therefore, the decrease of NO column density did not fully coincide with atmospheric transport.

Next, we evaluate the relationship between the NO variation and photochemistry. It is apparent that the temporal patterns of hours of darkness and NO column density are similar, as shown in Figure 4.2a. The correlation

coefficient between the duration of darkness and column density of NO was 0.9. The major mechanism responsible for NO production around ~100 km is the reaction of an excited nitrogen atom, $N(^2D)$, with an oxygen molecule:

$$N(^2D) + O_2 \rightarrow NO + O \quad (4.2)$$

where the excited nitrogen is produced mainly by auroral electrons through the reaction of a nitrogen molecule with a secondary electron and recombination of NO^+. The auroral impact is considered independent of the time of year. In contrast, solar radiation is strongly associated with processes that remove NO, such as

$$NO + h\nu \rightarrow N(^4S) + O \quad (4.3)$$

$$NO + N(^4S) \rightarrow N_2 + O \quad (4.4)$$

The main driver of the seasonal variation is therefore considered to be solar radiation, which determines the photochemical loss rate.

We compared our results with other NO observation results. *Baker et al.* [2001] have shown time series of daily averaged NO densities between 1998 and 2000 measured at an altitude of 106 km by the SNOE satellite. Even though the SNOE satellite observes only above an altitude of 100 km and cannot observe during the polar night, SNOE data show an annual cycle that is qualitatively very similar to our observations. The NO densities in the magnetic latitude range 60–70° evidenced seasonality in both hemispheres. The seasonal variations were more clearly apparent in the northern hemisphere, and the NO density in the northern hemisphere winter was about three times the NO density in the northern hemisphere summer. The seasonal trend and the NO density ratio between

summer and winter in their study are consistent with our observations.

Sheese et al. [2011] have shown, based on observations for more than 5 years, that the NO density during winter changes from year to year. They retrieved a time series of mean NO densities from NO_2 continuum data measured by the Optical Spectrograph and InfraRed Imager System (OSIRIS) satellite at altitudes of 90–100 km at high latitudes in the southern hemisphere during winter between 2003 and 2010. The largest increase of NO occurred in 2003, and the increment during winter gradually decreased toward the solar minimum of cycle 23. This previous result suggests that a decrease of the NO density toward the solar minimum will occur during the present solar cycle 24. We will therefore try to continue our NO observations from Syowa Station to investigate how the amplitude of the NO seasonal cycle changes as solar activity declines during the rest of solar cycle 24.

4.2 Short-term Variations of NO in a Timeframe of Several Days

4.2.1 Data analysis

In this section, we discuss variations of NO column densities on a time scale of several days. To extract such short-term variations, we first subtracted the seasonal variations expressed by equation (4.1) from the original NO column densities. The residuals are plotted in Figures 4.3e and 4.4e for 2012 and 2013, respectively. In these plots, significant positive values indicate short-term NO

enhancements that occurred in the altitude range 75–105 km. The error bars associated with individual data points indicate measurement errors, and the fitting error of the seasonal variation is also shown separately.

Figures 4.3 and 4.4 also show the time series of the Ap and Disturbance storm time (Dst) indices and the energetic proton and electron fluxes observed by the GOES-15 satellite. These data provide an overview of the relationship between short-term NO enhancement and solar activity. The energetic proton and electron fluxes are averages from the B detector of the GOES satellite, which faces either east or west. We used datasets to which a correction had been applied to remove contamination. We show the average flux of protons at an energy of 11.6 MeV in Figures 4.3c and 4.4c and the average flux of electrons at energies >0.8 MeV in Figures 4.3d and 4.4d.

It is apparent that short-term variations of NO roughly coincided with solar activities when the proton and electron fluxes were enhanced. Proton flux enhancements indicate the occurrence of SPEs. Electron flux enhancements are associated with magnetic storms and moderate solar activities. The designations “P-xx” and “E-xx” indicate a timeframe of 25 days, during which there was a SPE that caused the average flux of protons at an energy of 11.6 MeV to reach 10 cm^{-2} s^{-1} str^{-1} MeV^{-1}, and there was a geomagnetic storm with a minimum Dst of approximately –100 nT, respectively. Large geomagnetic storms with DST values of less than –100 nT were observed on 6 occasions during 2012 and twice during 2013. In Table 1 and 2, we summarized the basic characteristics of SPEs and geomagnetic storms and the increment of the NO column density for each designated period. Two circumstances satisfied both criteria: 1) the co-occurrence of a SPE and a geomagnetic storm, and 2) the precipitation of both electrons and protons. These two cases correspond to (P-II) and (P-III), respectively, in Figure

4.3, and to (E-I) and (E-IV), respectively, in Figure 4.4. In addition, (P-V) in Figure 4.3 partially overlapped with (E-VIII) in Figure 4.4. The majority of the electrons that contributed to the fluxes shown in Figure 4.3 and 4.4 were accelerated in the radiation belt during the recovery phase from a geomagnetic storm that corresponded to a gradual increase of the Dst index after an abrupt decrease. However, it should be noted that most of the electrons were “trapped” in the radiation belt, and the actual precipitating electron fluxes onto Syowa station were not equal to those measured by GOES, though the two fluxes were correlated with each other.

To explore the relationship between short-term variations of NO and the proton and electron flux enhancements in more detail, in Figures 4.5 and 4.6, we show relevant data during the 25-day timeframe designated as “P-xx” and “E-xx” in Figures 4.3 and 4.4. The Ap and Dst indices and the column densities of NO are the same as those in Figures 4.3 and 4.4. In addition, in order to derive flux values directly relevant to Syowa Station, we used proton and electron flux data obtained by low-altitude satellites, the NOAA POES, and the METOP-02 [*Evans and Greer*, 2000]. We show electron fluxes at energies >30 keV, >100 keV, and >300 keV, and proton fluxes in the energy ranges 0.8–2.5 MeV and 2.5–6.9 MeV recorded by the POES/METOP satellite in Figures 4.5 and 4.6. For each energy range, we used datasets obtained by the 0°- and 90°-pointing telescopes, which see roughly “precipitating” and “trapped” particles, respectively [*Rodger et al.*, 2010]. The process of data analysis is described in Appendix B. There are differences in the proton and electron fluxes recorded by the GOES and POES/METOP satellites because they observe at different magnetic lines and energies of proton and electrons. In the following discussions we have therefore compared the column density of NO with the proton and electron fluxes observed

by the POES/METOP 0°-telescopes (panels e and h in Figures 4.5 and 4.6), which see roughly “precipitating” particles over Syowa Station.

Table 4.1 List of solar proton event

	P-I	P-II	P-III	P-IV	P-V_a	P-V_b
Year	2012	2012	2012	2012	2013	2013
DOY of proton flux Max.	24	68	196	247	138	144
Day form proton flux Max. to NO max.	--	4	9	3	--	4
Max. NO column density (10^{15} /cm^2)	--	0.65	0.60	0.53	--	0.62

Table 4.2 List of geomagnetic storm

	E-I	E-II	E-III	E-IV$_a$	E-IV$_b$	E-V$_a$	E-V$_b$	E-V$_c$
Year	2012	2012	2012	2012	2012	2012	2012	2012
DOY of Dst min.	69	115	169	191	197	275	282	287
Dst min. (nT)	–118	–108	–71	–68	–118	–119	–95	–79
Day form Dst min. to NO max.	3	4	3	2	8	--	2	1
Max. NO column density (10^{15} /cm^2)	0.65	1.20	0.52	0.99	0.60	--	0.58	0.59

	E-VI	E-VII	E-VIII$_a$	E-VIII$_b$	E-VIII$_c$	E-IX$_a$	E-IX$_b$	E-IX$_c$	E-IX$_d$
Year	2012	2013	2013	2013	2013	2013	2013	2013	2013
DOY of Dst min.	319	76	145	152	158	180	187	191	195
Dst min. (nT)	–108	–132	–55	–119	–73	–98	–79	–47	–72
Day form Dst min. to NO max.	--	--	3	1	1	--	--	--	0
Max. NO column density (10^{15} /cm^2)	--	--	0.62	0.46	0.70	--	--	--	0.93

4.2.2 Discussion

It is apparent from Figures 4.3 and 4.4 that short-term enhancements seem to be related to solar activities, that is, SPEs and geomagnetic storms. During SPEs such as (P-II), (P-IV), and (P-V), significant NO enhancements were seen, whereas during (P-I) the NO increment was marginal, although there was a huge

proton flux, the highest during the nearly two-year observation period. In contrast, it is remarkable that some NO enhancements occurred during periods without SPEs. The NO enhancement during (E-II) was the most prominant event during the observation period, and one of the best examples of such non-SPE NO enhancements. The (E-IX) event is another clear example of non-SPE NO enhancements. These events clearly showed that energetic electrons play an important role in the short-term, in situ enhancement of NO in the 75–105 km altitude range above Syowa station.

The variablities of the geomagnetic indices and the proton and electron fluxes were larger in 2012 than in 2013. The larger scattering of the NO column density anomaly in 2012 (Figure 4.3e) than in 2013 (Figure 4.4e) could reflect the higher solar activity in 2012. Because we fitted the seasonal variation with a sinusoidal function with the same amplitude for both years, the fact that the deviation from the fitted function tended to be large in 2012 suggests that there was more solar activity in 2012 than in 2013.

More details become apparent if each case is examined relative to the proton fluxes and Dst indices. We first discuss the variation of NO during the SPE shown in Figure 4.5. We were unable to find a large enhancement of the NO column density, which reached only 0.5 (10^{15} cm^{-2}), during significant proton precipitation. Cases (P-I) and (P-II) were associated with large SPEs, during which the proton flux reached 10^4 (cm^{-2} s^{-1} str^{-1}), but the column density of NO reached only ~0.5 (10^{15} cm^{-2}). These cases occurred in the summer and fall, and the photoperiods were longer than the scotoperiods. The photochemical destruction of NO may therefore have been more effective in both cases, as we discussed in section 4. However, even in cases (P-IV) and (P-V), during both of which the photoperiod was much smaller than in cases (P-I) and (P-II), the

column density of NO was still about the same, ~0.5 (10^{15} cm^{-2}). Photochemical loss may therefore not explain why the NO enhancements in (P-I) and (P-II) were not very remarkable. Except for (P-I), (P-IV), and possibly (P-II), the temporal coincidence between the SPE and NO enhancements was not very clear. During the (P-V) period, two proton precipitation events occurred, but the associated NO enhancement was apparent during only one of the two events. During the (P-III) event, the NO data are unfortunately missing during the period of SPE because of bad weather. The fact that the first NO enhancement occurred before the SPE suggests that this NO enhancement was independent of the SPE, and the second NO enhancement apparently began after the termination of the SPE. In contrast, examination of the "precipitating" electron fluxes indicated in Figure 4.5f indicates that the correlation with the NO column densities is slightly better. During the (P-III) period, there were high electron fluxes corresponding to the two NO enhancements. For the (P-V) case, there was an electron precipitation around DOY 140, but still no enhancement of NO. However, during the period of NO enhancement around DOY 145–150, the electron flux was larger than the previous precipitation. Even for the (P-II) and (P-IV) events, during which the SPE and NO were more-or-less coincident, the precipitating electron flux was also high during the NO enhancements. These data suggest that precipitation of energetic electrons may be a major cause of NO enhancements, even during SPEs, though we cannot deny the possible contribution of solar protons above Syowa station.

We next discuss NO variations during a geomagnetic storm, i.e. the relationship between the precipitating electrons and NO (Figure 4.6). The enhanced column densities of NO in the summer, [e.g., cases (E-I), (E-V), (E-VI), and (E-VII) in Figure 4.6], were about 0.5 (10^{15} cm^{-2}). In winter, however [e.g., cases (E-II), (E-IV), and (E-IX) in Figure 4.6], column densities of NO reached about 1.0 (10^{15}

cm^{-2}). The implication is that the photochemical destruction of NO is more effective in the summer, as discussed in section 4. In cases (E-II), (E-III), (E-IV), (E-VIII), and (E-IX) (Figure 4.6), there was a consistent pattern in the variation of the NO column density. The NO short-term enhancement peaked 1–5 days after the onset of the geomagnetic storm and terminated within 5–10 days. *Newnham et al.* [2011] have reported that the mesospheric NO volume-mixing ratio at 70–80 km gradually increased over 3–4 days. Our results are consistent with their study; 1–5 days were required to reach the maximum NO column density.

Case (E-II) was a very simple and clear single event in which the NO column density began to increase during the recovery phase and peaked on DOY 119 in 2012, which was 4 days after the main phase of the storm. During this period, fluxes of electrons with energies >30 keV increased to 10^6 (cm^{-2} s^{-1} str^{-1}), but proton fluxes remained at the noise level. In chapter 5, we provide a more detailed discussion of the NO variation in case (E-II) based on 3-h-average, high temporal resolution data. Cases (E-VIII) and (E-IX) are similar cases, during which electron fluxes increased but proton fluxes remained at the noise level. In case (E-VIII) we found three peaks of the column density of NO that corresponded to three storms. These peaks occurred 1–3 days after the main phase of the storm. In case (E-IX), three other storms occurred between DOY185 and DOY 200 in 2013, but we found only one peak of NO column density. The implication is that variations of NO due to closely spaced storms may be complex.

During cases (E-III) and (E-IV) there were increases of both proton and electron fluxes. The NO enhancements in cases (E-III) and DOY 191 of (E-IV) were regarded related mainly to electron precipitation because of the relatively small proton fluxes less than 10^3 (cm^{-2} s^{-1} str^{-1}) and ~10^2 (cm^{-2} s^{-1} str^{-1}), respectively. While the proton flux is ~10^4 (cm^{-2} s^{-1} str^{-1}) around DOY 197 of

(E-IV), there were no NO data unfortunately. There were no observations during DOY 165 – 170 of (E-III), and we found only a partial enhancement with subsequent gradual decrease. However, we found NO enhancements with subsequent gradual increase and decrease around DOY 193 and 205 in case (E-IV). The NO enhancement around DOY 193 was associated with a geomagnetic storm on DOY 191, and it peaked 2 days after the onset of the geomagnetic storm. Another NO enhancement around DOY 205 peaked 8 days after the onset of the geomagnetic storm on DOY 197. We believe that this enhancement was associated with substorms during the end of the recovery phase of the storm. The AL index reached –600 nT and –400 nT on DOY 202 and 205, respectively (not shown).

In Figure 4.7, we show correlation diagrams between the NO column density and the proton and electron fluxes. In this figure, the proton and electron fluxes are daily averaged values. There was no significant correlation between NO column density and proton flux (Figure 4.7a). There was, however, a weak correlation between the NO column density and the precipitating electron flux above an electron flux of $10^{3.5}$ (cm^{-2} s^{-1} sr^{-1}), though there was no correlation below this flux. The correlation coefficient was 0.33, and t-value of statistical t-test is 5.1 for 218 data points, suggesting the correlation is significant at 99% confidence. The flux of $10^{3.5}$ (cm^{-2} s^{-1} sr^{-1}) is a kind of empirical flux threshold, above which a significant enhancement of the NO column density above the noise level of the present observation. . The possible reasons for the large amount of scatter include the effects of other NO production and loss mechanisms such as photochemistry, inappropriateness of the seasonal fitting curve for subtracting the seasonal component from the original derived NO column density, and uncertainty in the temperature, which we assumed to be a constant equal to 200 K in this study.

Though the correlation coefficient was weak, we believe the significance of the correlation above an electron flux of $10^{3.5}$ (cm^{-2} s^{-1} sr^{-1}) suggests that electron precipitation has a greater influence on the NO column density than solar proton fluxes above Syowa station.

We have discussed short-term variations in this section. We believe that electron precipitation was more effective than proton precipitation for NO enhancement in the altitude range 75–105 km. During the SPE in January and March 2012, the column density of NO reached only ~0.5 (10^{15} cm^{-2}), even though the proton flux was more than 10^4 (cm^{-2} s^{-1} str^{-1}). However, the column density of NO reached more than ~ 1.0 (10^{15} cm^{-2}) during a geomagnetic storm when the flux of electrons with energies >30 keV was 10^6 (cm^{-2} s^{-1} str^{-1}).

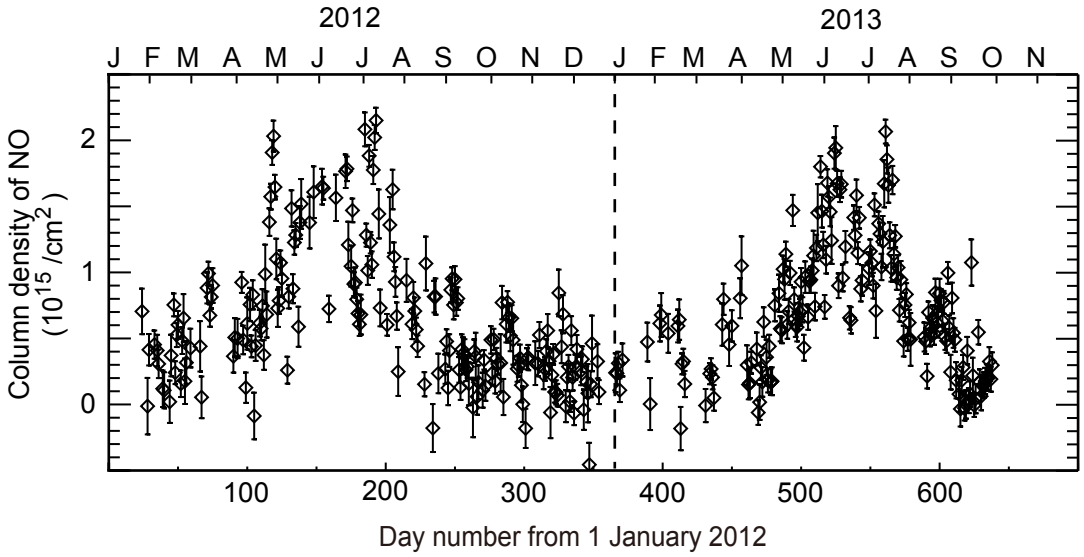

Figure 4.1 Time series of the daily column density of NO in the altitude range 75–105 km. Error bars indicate the rms noise.

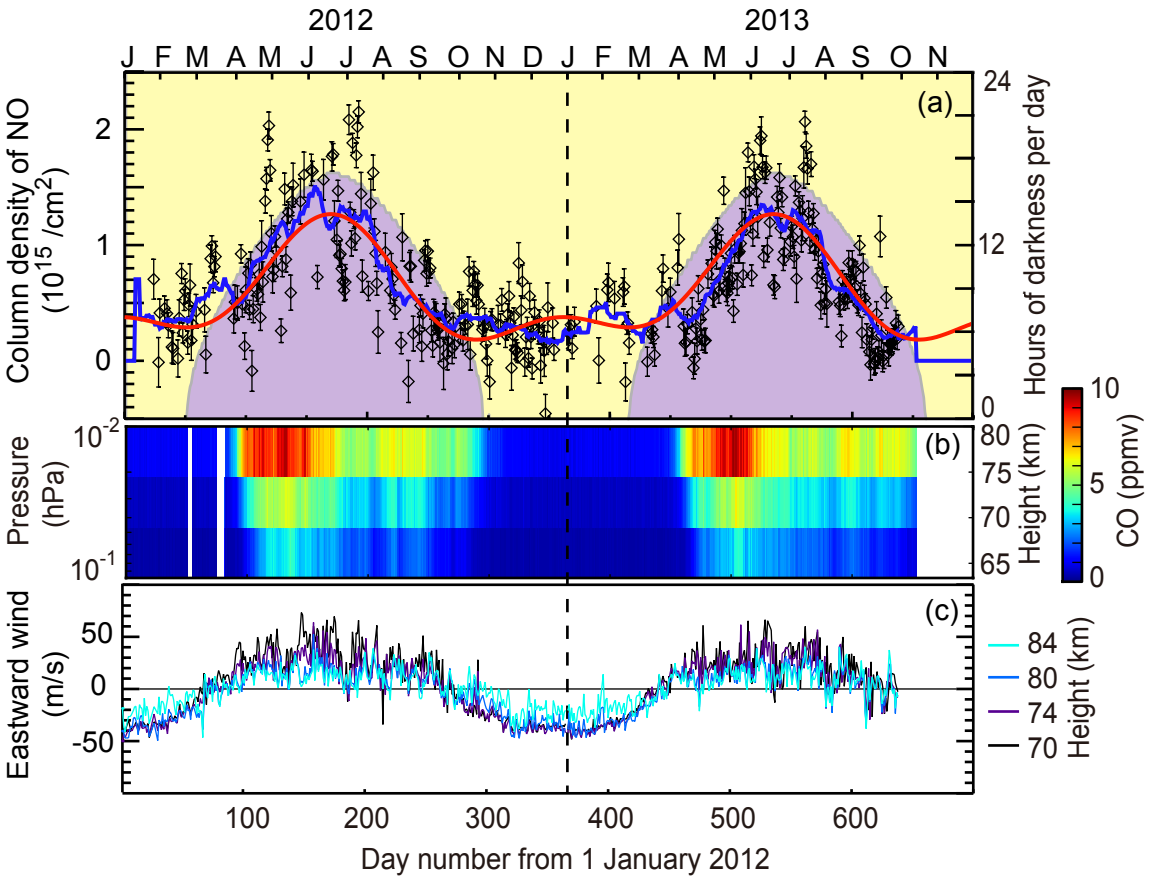

Figure 4.2 (a) Same as Figure 4.1 but with blue and red curves superimposed that indicate 31-day running averages and a sinusoidal function consisting of annual and semi-annual periodic component, respectively. The sinusoidal function was fit by least squares. The right-hand axis is time in hours. Purple and yellow shading indicates the length of night and day, respectively, at an altitude of 100 km. (b) Vertical profile of CO observed by the Aura/MLS. We calculated the daily average CO vertical profile by using data at latitudes between roughly –65° and –75°, longitudes between –180° and 180°, and pressures between 0.1 hPa and 0.01 hPa. (c) Eastward wind speed observed by MF radar at Syowa Station. Black, purple, blue, and light blue lines indicate wind speeds of 70 km h^{-1}, 74 km h^{-1}, 80 km h^{-1}, and 84 km h^{-1}, respectively.

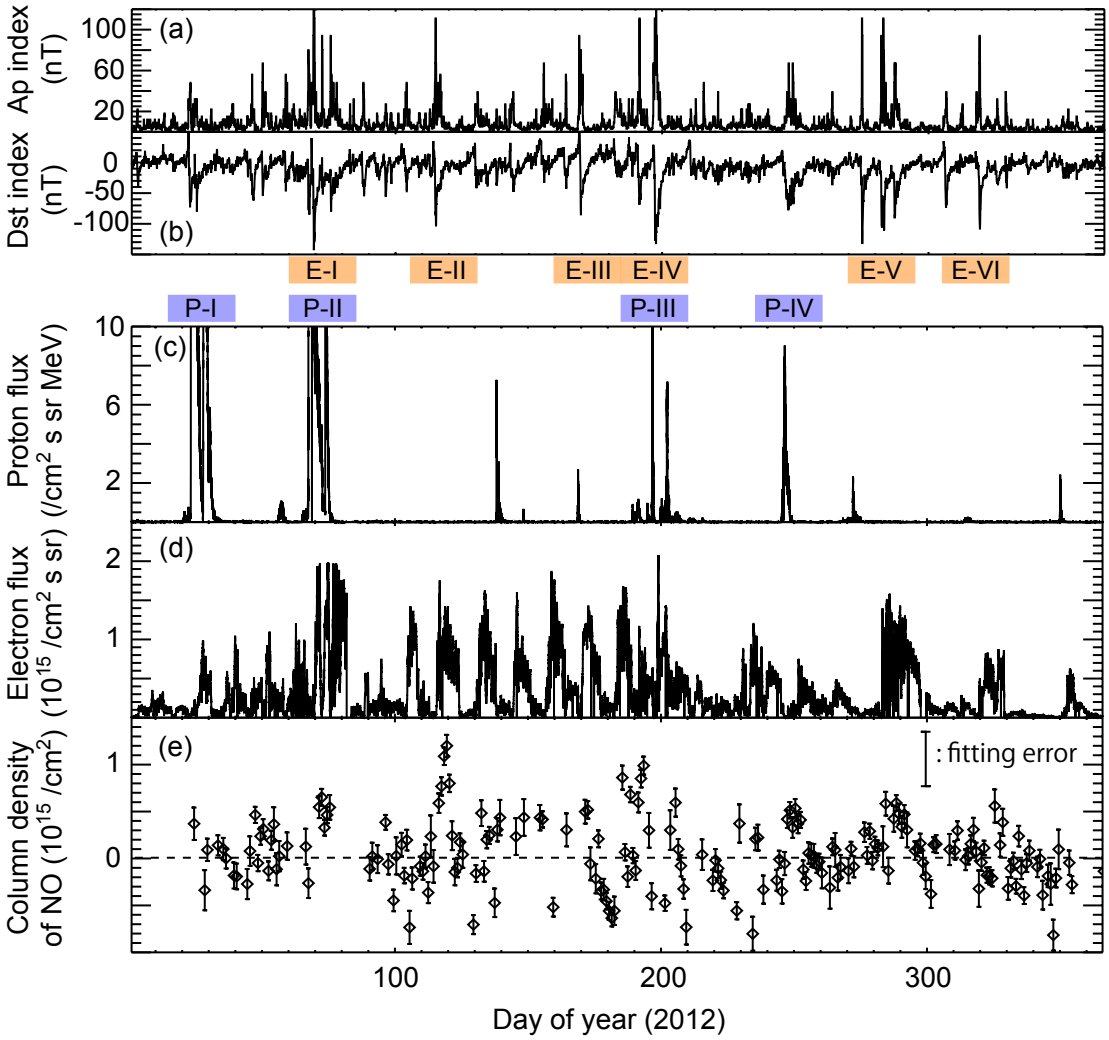

Figure 4.3 Time series in 2012 of (a) Ap index (nT), (b) Dst index (nT), (c) average proton flux (cm^{-2} s^{-1} str^{-1} MeV^{-1}) at energy of 11.6 MeV observed by the GOES-15 satellite, (d) average electron flux (cm^{-2} s^{-1} str^{-1}) at energies >0.8 MeV observed by the GOES-15 satellite, and (e) the column density of NO (10^{15} cm^{-2}) after subtraction of seasonal variations. Signs of "P-xx" and "E-xx" indicate the selected timeframes which are shown in Figure 4.5 and 4.6.

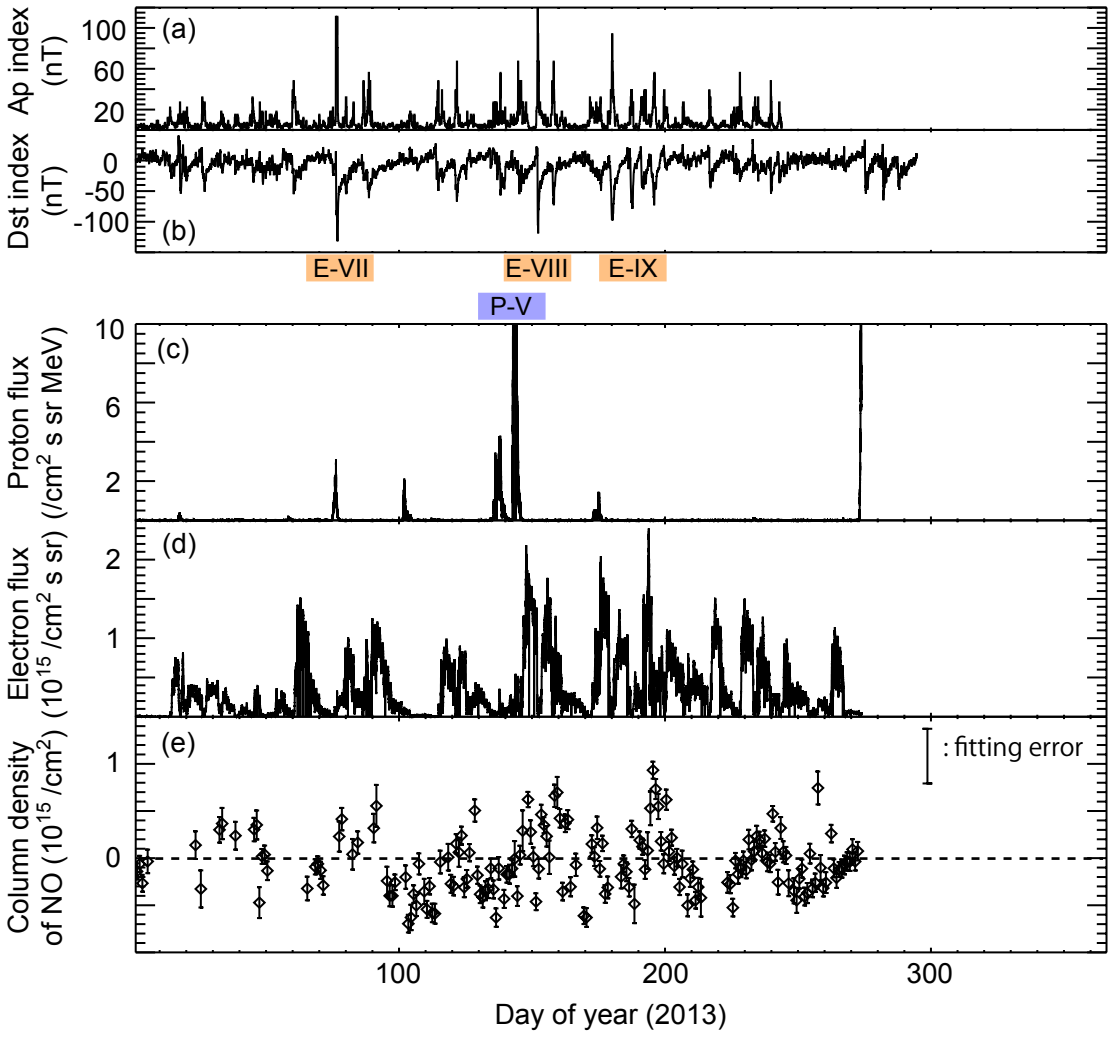

Figure 4.4 Same as Figure 4.3, but in 2013 (until 30 September; DOY 273).

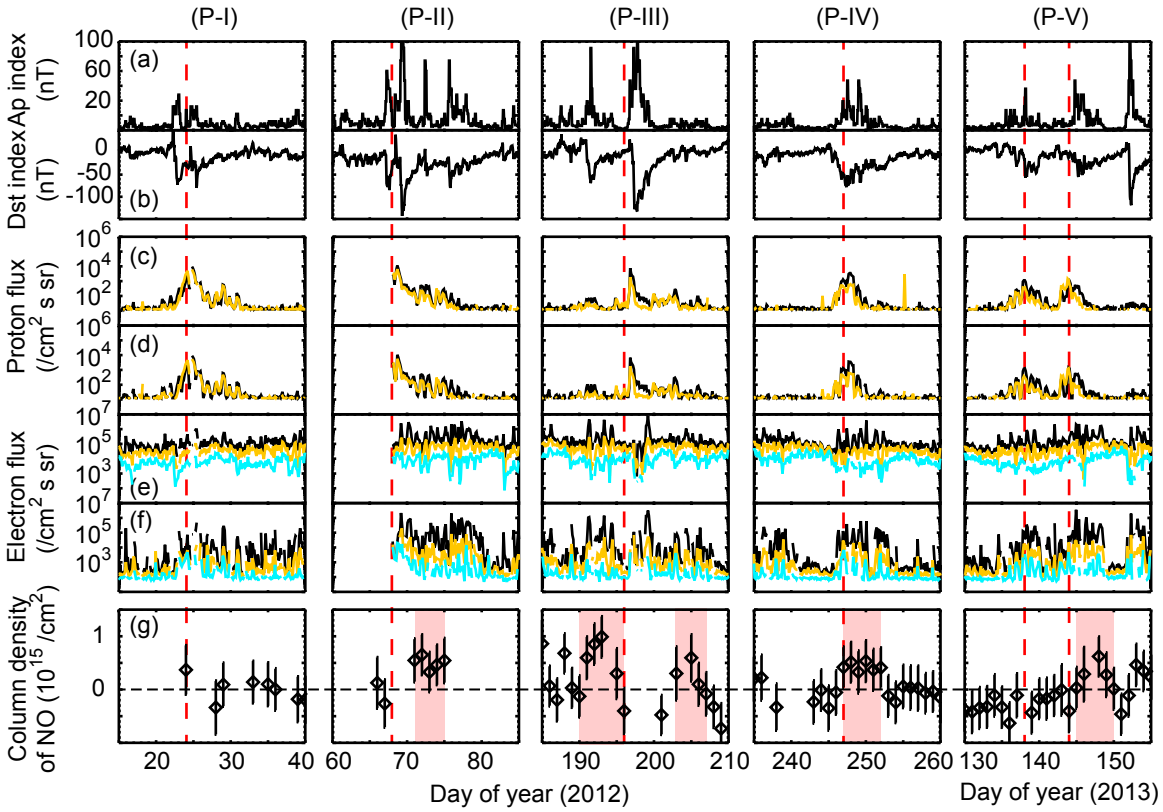

Figure 4.5 The 25-day time series during a SPE event when the average flux of protons at energy of 11.6 MeV reached 10 (cm^{-2} s^{-1} str^{-1} MeV^{-1}) in 2012 and 2013. (a) Ap index (nT), (b) Dst index (nT), (c) and (d) proton fluxes (cm^{-2} s^{-1} str^{-1}) in the energy ranges 0.8–2.5 MeV (black) and 2.5–6.9 MeV (orange) observed by the 90° and 0° telescopes, respectively, on the POES/METOP, (e) and (f) electron fluxes (cm^{-2} s^{-1} str^{-1}) in the energy range >30 keV (black), >100 keV (orange), and >300 keV (blue) observed by the 90°- and 0°-telescope on the POES/METOP, respectively, and (g) the column density of NO (10^{15} cm^{-2}), after subtraction of the seasonal variation. Red dashed lines indicate day of peak proton flux which is daily averaged.

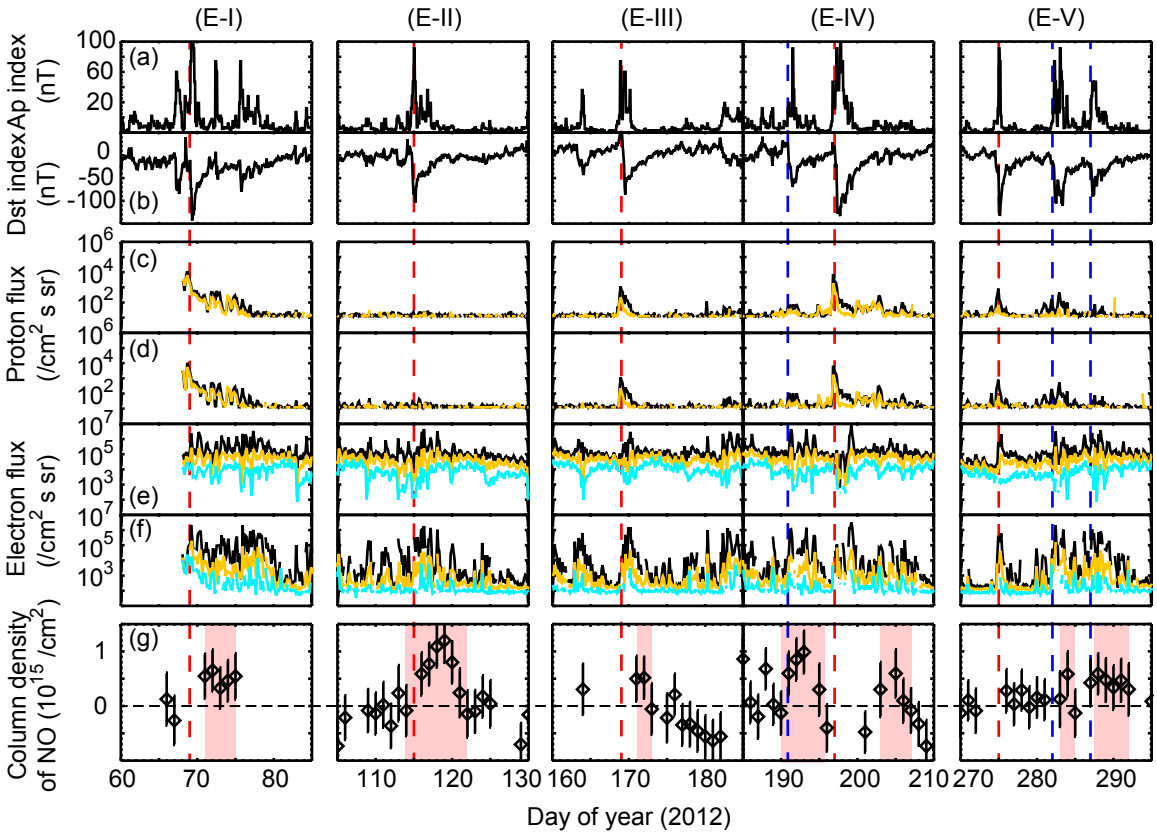

Figure 4.6 The 25-day time series during the geomagnetic storm when Dst was about –100 nT in 2012 and 2013. (a) – (g) have the same meaning as in Figure 4.5. (E-I) and (E-IV) have a meaning similar to (P-II) and (P-III) in Figure 4.5, respectively.Red and blue dashed lines indicate day of minimum Dst index value which is daily averaged.

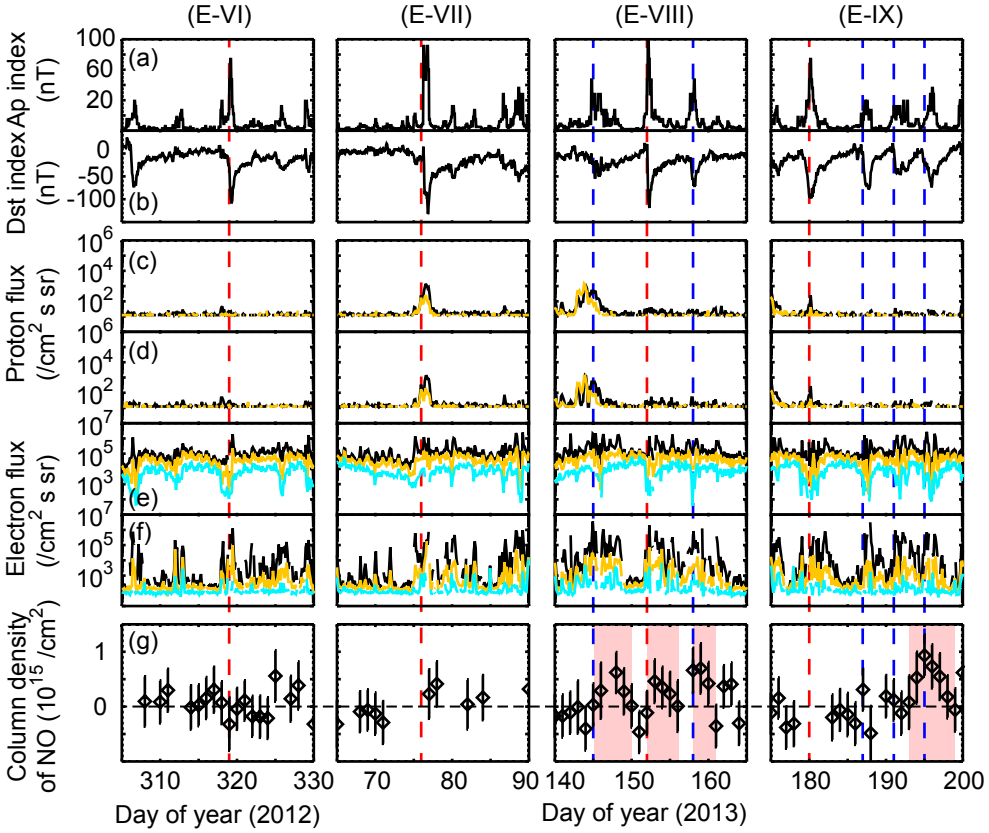

Figure 4.6 (Continued)

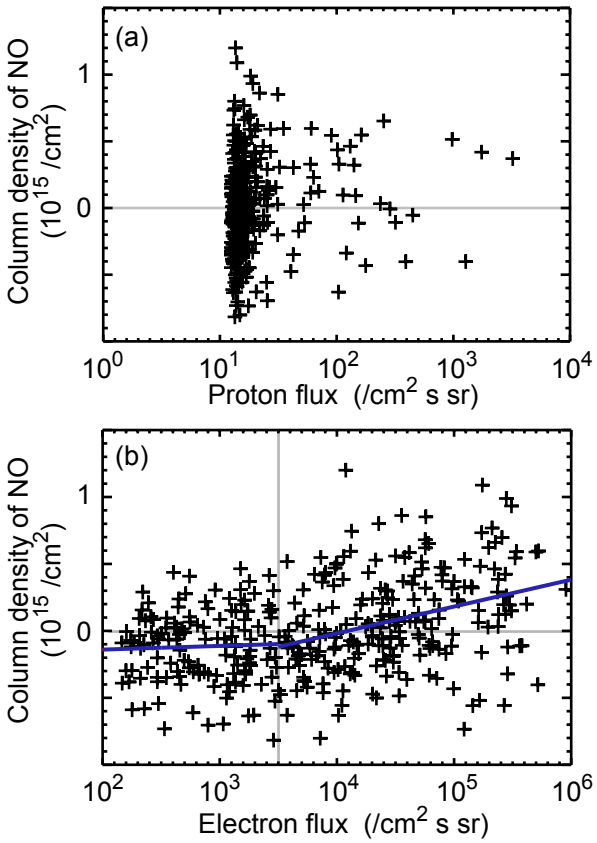

Figure 4.7 The column density of NO versus daily averaged proton flux (upper) and electron flux (lower). Blue lines indicate liner approximation. The column density of NO is subtracted seasonal variation. And it is plotted all of NO observed data as shown in Figure 4.3 and 4.4. Electron fluxes are in the energy range >30 keV and proton fluxes are in the energy ranges 0.8–2.5 MeV observed by the 0° telescopes on the POES/METOP.

Chapter 5

Typical single event in April 2012

In this chapter, we focused on a NO enhancement event related to a geomagnetic storm that occurred in April 2012 (Case E-II in Figure 4.6). This was the most prominent NO enhancement event which is 3 times larger than ordinary values observed above Syowa Station in 2012. We were able to investigate the NO variation associated with the geomagnetic storm during one day at a temporal resolution of 3 hours. Most observations of this event were made without attenuation of the NO emissions by snow and frost.

5.1 Results

Figure 3.3a shows the 24-h-averaged spectrum of NO at 250.796 GHz on 29 April 2012 (DOY 120). All of the other daily NO spectra obtained between DOY 110 and DOY 124 were similar to the spectrum on DOY 120. The rms noise of daily NO spectra ranged between 14 mK and 35 mK, depending on the total

observation time.

Figure 5.1 shows a time series of the NO column density from DOY 110 to DOY 124; the AP, Dst and AL indices; and the electron and proton fluxes observed by the POES/METOP and GOES-15. A large geomagnetic storm occurred on 24 April 2012 (DOY 115), and the minimum value of the Dst index was –104 nT during the main phase (Figure 5.1a). On DOY 118, after the recovery phase, values of the Dst and Ap indices were almost zero. The values of the AL index (Figure 5.1b) reached about –1000 nT and –600 nT during the main phase and the recovery phase, respectively. Several substorms occurred on DOY 118 and DOY 120 after the storm recovery phase.

The 3-h averaged NO column densities are shown in Figure 5.1c. Note that the observations depend on the weather condition at Syowa Station: observations of NO spectra were not possible during the main phase of the magnetic storm because of a blizzard. The column density of NO gradually increased during the recovery phase between DOY 116 and DOY 120 and suddenly decreased from 4.0 to 1.0 ($\times 10^{15}$ cm^{-2}) during the afternoon of DOY 120.

In addition to variations on a timeframe of several days, we found diurnal variations, such as a doubling at UT 0 on DOY 118 and DOY 120, and smaller increases at UT 0 on DOY 117 and DOY 119. These diurnal variations are discussed in more detail in the next section.

It is remarkable that the flux of protons recorded by the GOES-15 at energies >11.6 MeV remained below the noise level throughout this event (Figure 5.1f). Figures 5.1g and 5.1h show the fluxes of protons over Syowa Station with energies 800-2500 keV and 2500-6900 keV recorded by the 90° and 0° telescopes on the POES/METOP which described the procedure in Appendix A. Those proton fluxes were also almost the same as the noise levels throughout this event.

In contrast, the electron flux showed significant variability. Figures 5.1d and 5.1e show the fluxes of electrons with energies >30 keV, >100 keV, and >300 keV observed by the 90° and 0° telescopes on the POES/METOP. The trapped flux of 300 keV electrons was gradually recovered after the drop out of the storm main phase, which is typical variation of the outer belts during storms [e.g., *Miyoshi and Kataoka*, 2005]. On the other hand, transient enhancements of the precipitating flux were seen in the main and recovery phases of this storm.

Figure 5.1i shows correlation coefficients between the column density of NO and the electron flux observed by the 90° telescope during the period between DOY 116.5 and DOY 120.5. We used only the 90° telescope data because strong contaminations of the 0° telescope have been known [*Rodger et al.*, 2010]. The results show that the maximum value of the correlation coefficient between the column density of NO and electron fluxes observed by the 90° telescope were between 0.4 and 0.45, and the lag time was less than 1 h (Figure 5.1i).

5.2 Discussion

We have presented the temporal variation of the column density of NO associated with a geomagnetic storm that occurred on DOY 115 in 2012. During the storm, the flux of protons with energies >11.6 MeV observed by the GOES satellite was below the sensor's detection limit which was ~10^{-2} cm^{-2} s^{-1} str^{-1} MeV^{-1}. The fluxes of protons with energies 800-2500 keV and 2500-6900 keV observed by the POES/METOP were almost the same as the noise levels which was ~10^{1} cm^{-2} s^{-1} str^{-1} for both. It is hard to consider that protons affected the

temporal variation of NO. On the other hand, energetic electrons were precipitated intensively into Earth's atmosphere.

We observed a significant increase and decrease of the column density of NO. The maximum value of the column density of NO was 4×10^{15} cm^{-2} on DOY 120, five days after the main phase of the geomagnetic storm. *Newnham et al.* [2011] have reported that the mesospheric NO volume mixing ratio at 70–80 km showed a gradual buildup over 3–4 days and that the NO was produced directly by the precipitation of >300 keV electrons. The gradual build up indicated that the NO production is competing strongly against day-time losses rather than an immediate increase with electron flux. Our results are consistent with their study; five days were required to reach the maximum NO column density. After reaching a maximum, the NO column density suddenly decreased in the afternoon on DOY 120, which corresponds to a decrease of electron flux apparent in the 0° telescope data, and the flux in the 0° telescope kept low level until DOY 123 (Figure 5.1e).

However, the gradual increase of NO column density in the recovery phase was not monotonic; instead, some additional diurnal features were apparent. In this section, we discuss the diurnal variation of NO and its possible causes.

First, major chemical reactions between NO and NO_2 in the mesosphere may have caused diurnal variations (equations (1.12)-(1.15)). As shown in section 1.4, most NO is converted into NO_2 at night in the altitude range below ~75 km, when there is no solar radiation and less of the reactant O. During the daytime, solar radiation restores NO. In contrast, in the altitude range between 75 km and 110 km, there is almost no diurnal variation. During the event we studied, the approximate times of sunrise and sunset were 5:30 UT and 13:00 UT, respectively, at the end of April at Syowa Station. However, the variation of the column density of NO did not correspond to these sunrise and sunset times (Figure 5.1c), and the

column density of NO remained at a high level (>2 × 10^{15} cm^{-2}) throughout the day during the recovery phase, the suggestion being that photochemical reactions contributed little to the observed NO variations.

Second, the temporal variation of NO was more likely related to energetic electron precipitation rather than to solar radiation between DOY 116 and DOY 120, and it is noteworthy that the altitudes of maximum ionization rates by mono-energetic ~30 keV and ~300 keV electrons were approximately 90 km and 70 km, respectively [*Turunen et al.*, 2009]. There was a positive correlation between the column density of NO and electron flux within 1 h (Figure 5.1i). In addition, a one-to-one correspondence was apparent between the tendencies for both the NO column density and the electron flux to increase at UT 0 on DOY 117, 118, 119, and 120 (Figure 5.1c, 5.1d, and 5.1e). The amplitudes of the increases of the NO column density and electron fluxes are not in complete quantitative agreement in these comparisons, but quantitative comparisons may be confounded by the incompleteness of the currently available datasets. Indeed the “precipitating” flux measurements by the 0° telescopes are strongly contaminated by low-energy protons [*Rodger et al.*, 2010]. In addition, the electron flux data were obtained discontinuously by the orbital satellite and are mean values of some representative points within 3-h bins rather than averages of continuous sampling data.

These tendencies of the column densities and fluxes of 30 keV electrons to increase at UT 0 can be interpreted in terms of the enhanced precipitation of the plasma sheet electrons. Figure 5.2 shows the MLT-UT temporal dependence of the electron fluxes observed by the POES/METOP at energies >30 keV. It is clear that the plasma sheet electrons were enhanced toward dawn [e.g., *Miyoshi et al.*, 2013] because of the magnetic drift of energetic electrons, and the resultant dawn-dusk asymmetry is apparent. The electron flux increased because of the sub-storms on

DOY 118 and DOY 120. Syowa Station passed through a dawn-dusk asymmetry, as shown by the white lines in Figure 5.2, and we observed a remarkable increase of NO near dawn at Syowa Station.

The rapid response (within 1 h) and one-to-one correspondence between NO column densities and electron fluxes are convincing evidence that precipitated electrons played an important role in NO production; a series of processes that enhanced the amount of NO associated with precipitated electrons occurred as soon as the electrons precipitated in the altitude range between 75 km and 105 km.

Finally, there is another probable cause of enhancement of NO with a delay on a timeframe of hours. Effects of horizontal advection always exist. The eastward wind velocity observed by MF radar at Syowa Station [*Tsutsumi et al.*, 2001] was approximately 20 m s^{-1} at altitudes of 75–105 km; the northward wind velocity was smaller than the eastward velocity during this period. Although an eastward wind could transport NO-rich air, this velocity is too slow to transport NO-rich air from the night side to the day side within one day.

At Syowa Station, the environment of Earth's atmosphere is measured with various instruments. The Program of the Antarctic Syowa MST/IS Radar (PANSY) [*Sato et al.*, 2013] has been used to observe vertical winds from the troposphere to the mesosphere since April 2012. Rayleigh-Raman Lidar [*Suzuki et al.*, 2012] has been used to observe the temperature between 15 km and 80 km since 2011. We plan to collaborate with these programs and to investigate the influence of the downward transport of NO_x due to the polar vortex.

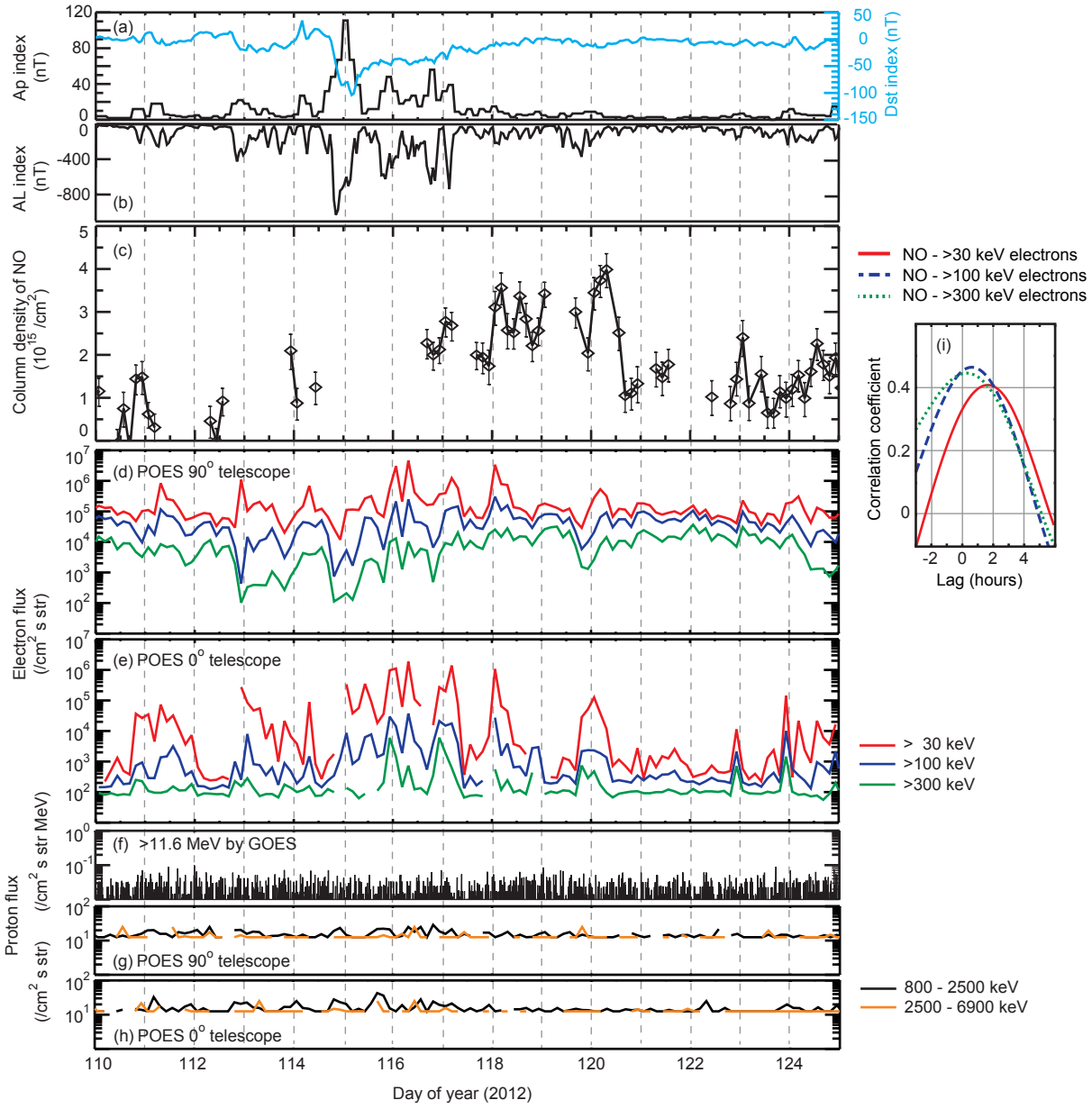

Figure 5.1 Time series of (a) Ap (black), Dst (aqua blue), and (b) AL indices (nT), (c) the column density of NO (10^{15} cm^{-2}), (d) and (e) the electron flux (cm^{-2} s^{-1} str^{-1}) in the energy range >30 keV (red), >100 keV (blue), and >300 keV (green) observed by 90° and 0° telescope on the POES/METOP, respectively, (f) the proton flux (cm^{-2} s^{-1} str^{-1} MeV^{-1}) in the energy range >11.6 MeV observed by GOES-15 during the time of a large geomagnetic storm on 24 April 2012 (DOY 115), and (g) and (h) the proton fluxes (cm^{-2} s^{-1} str^{-1}) in the energy range 800-2500 keV (black) and 2500-6900 keV (orange) observed by 90° and 0° telescope on the POES/METOP, respectively. (i) Correlation coefficient between the column density of NO and electron fluxes observed by 90° telescope. The red, blue and green lines correspond to energy ranges of >30 keV, >100 keV and >300 keV, respectively, for the electron flux.

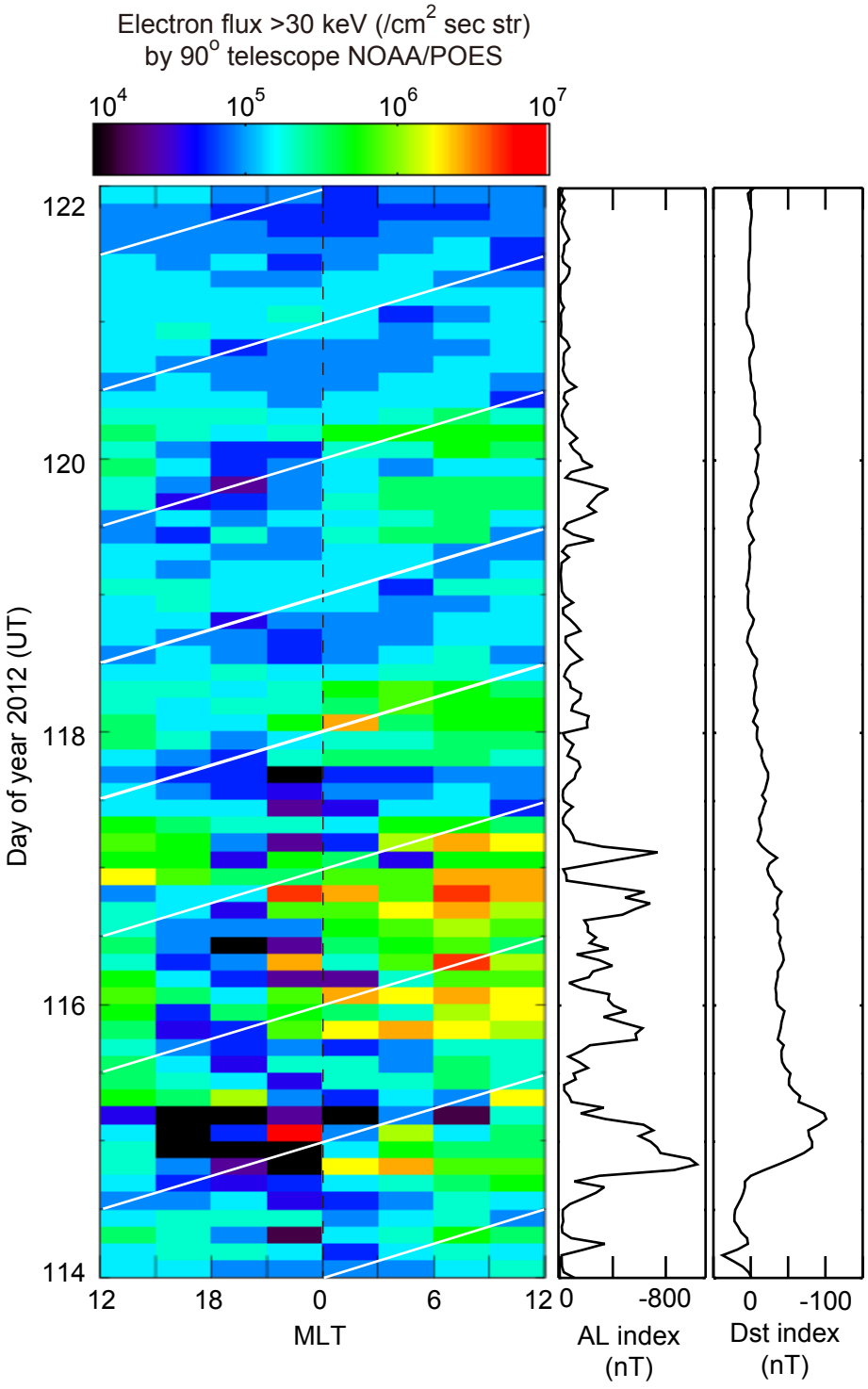

Figure 5.2 (Left) The MLT-UT time dependence of the flux of electrons with energies >30 keV observed by the 90° telescope on the POES/METOP between DOY 114 and DOY 122. The color scale indicates the electron flux on a log scale (cm^{-2} s^{-1} str^{-1}). White lines indicate the trace of Syowa Station. (Right) AL and Dst indices (nT) between DOY 114 and DOY 122.

Chapter 6

Conclusions

We observed the spectrum of NO at 250.796 GHz with the ground-based millimeter-wave spectroscopic radiometer at Syowa Station, Antarctica. We used the NO spectrum line shape and NO column density relationship with solar radiation to determine that NO emissions occurred at altitudes of 75–105 km.

Examination of time series observations, from 2012 to 2013, revealed both seasonal variations and short-term variations (on a timeframe of several days). During the seasonal variations, the column density of NO during the winter was about four times the column density during the summer. The main driver of the seasonal variation is considered to be solar radiation, which determines the photochemical loss rate, since the temporal patterns of NO column density and hours of darkness show good correlation with each other. We were able to clearly discern short-term enhancement events by subtracting the seasonal pattern from the original NO column densities. Analysis of a 25-day time series that included SPEs and geomagnetic storms revealed that short-term variations of NO were caused mainly by precipitation of energetic electrons associated with geomagnetic storms rather than by SPEs above Syowa station. The column density of NO

reached more than 1.0 (10^{15} cm^{-2}) during a geomagnetic storm, during which the flux of electrons with energies >30 keV was 10^6 (cm^{-2} s^{-1} str^{-1}). When the electrons precipitated, the column density of NO gradually increased during the recovery phase of the storm and then gradually decreased. In addition, the NO column density peaked 1–5 days after the onset of a geomagnetic storm and terminated within 5–10 days. Correlation analysis between the NO column density and the proton and electron fluxes indicates that there are weak but significant correlation between the NO and the electron flux above $10^{3.5}$ (cm^{-2} s^{-1} sr^{-1}) but no correlation between the NO and the proton flux. This also suggests that electron precipitation has a greater influence on the NO column density than solar proton fluxes above Syowa station in the auroral region, even during SPEs. Case (E-II) was a very simple and typical single event in which the NO column density began to increase during the recovery phase and peaked on DOY 119 in 2012, which was 4 days after the main phase of the storm. According to high temporal resolution data, we found that the column densities of NO were related to precipitated electrons observed by the POES/METOP satellites in the energy range 30–300 keV. The NO column densities were enhanced within one hour following precipitation of electrons. For the first time, we identified a remarkable increase of the column density of NO at UT 0, which was caused by the dawn-dusk asymmetry of plasma sheet electrons, suggesting that tens keV electrons are essential to cause the variation of the column density of NO.

Although it was difficult to quantitate of NO vertical profile in present analysis, we found some difference with effects of SPE in previous studies that report the intensive NO enhancement was expanded in geomagnetic latitude with >60°. This observation would contribute to accurate estimations of NO variation.

Future works

- **Loss processes of NO**

In this thesis, we discussed mainly production of NO by EPP. However loss processes due to EPP were also occurred at the same time. The slightly increase of NO during SPE may relate a balance between production and loss. On the other hand, NO is attenuated by solar radiation. Intensity of solar radiation fluctuate with seasons i.e., solar zenith angle. We have to consider not only hours of darkness/sunlight at 100 km but also intensity of solar radiation. In the future, we will estimate loss processes depend on EPP and intensity of solar radiation. And we will simulate variations of NO by model in the mesosphere and lower thermosphere.

- **Other possible cause of NO enhancement**

We have reported clearly NO increase during geomagnetic storm and slightly increase during SPE in this thesis. We concluded that NO increase mainly depended on energetic electrons. However, it may need other detail conditions. We want to clarify it by recent observation data (after 9/30 2013), the collaboration with other observations.

- **Effect of diffusion**

The eastward wind and turbulent diffusion always exit in the mesosphere and thermosphere at the polar region. The increased NO may be transport and averaged under the influence of these. We will consider these effects by using radar and climate models.

- **Relation to diffuse aurora**

When diffuse aurora occurs, high energy electrons also precipitate. We will compare high time resolution data of NO with all sky camera data at Syowa Station, and we will consider these relations such as spatial position. Unfortunately, we did not obtain all sky camera data at Syowa Station during recovery phase of geomagnetic storm on April 2012, i.e., DOY117-121.

- **Future plans of observation**

First, we want to set up our observation system at other places. Dome Fuji is located inland of Antarctica, and geomagnetic latitude is 71°. We consider that Dome Fuji is affected by solar proton rather than Syowa Station because of high geomagnetic latitude. We will be able to reveal the influence of solar proton and compare difference of the NO variation between Syowa Station and Dome Fuji. We also want to try conjugate observation in Iceland. We will detect opposite seasonal variation and similar short-term variations. We want to reveal other factors of NO increase from the difference with these predicted results.

Second, we want to collaborate with other observations. At Syowa Station, the Program of the Antarctic Syowa MST/IS Radar (PANSY) has been used to observe vertical winds from the troposphere to the mesosphere, and Rayleigh-Raman Lidar has been used to observe the temperature between 15 km and 80 km. In both hemispheres, SuperDARN (Super Dual Auroral Radar Network) radar observes the two-dimensional distribution of the plasma drift in the ionospheric region. We will compare these physical quantities with the column density of NO, and reveal detail conditions of NO variations.

Appendix A: Low Altitude Satellite Observations

In this appendix, we describe the process of POES/METOP data analysis. We used electron fluxes at energies of >30 keV, >100 keV and >300 keV, and we used proton fluxes in the energy ranges 0.8–2.5 MeV and 2.5–6.9 MeV recorded by the POES/METOP satellite in Figures 4.5 and 4.6. For each energy range, we used datasets obtained with the 0°- and 90°-pointing telescopes, which see roughly "precipitated" and "trapped" electrons, respectively [*Rodger et al.*, 2010]. To compare the precipitation flux of energetic particles with the NO column density above Syowa station, we selected and combined the datasets by using the following criteria.

First, we chose the data between McIlwain L-parameters of 5.47 and 6.49, which correspond to the invariant latitudes between 64.7° and 66.9° in the northern and southern hemispheres. We divided those selected datasets into sub-dataset bins determined on the basis of universal time (UT) and magnetic local time (MLT) for each time and longitudinal axis, respectively. The resolution of the UT and MLT was 3 hours for each, and we calculated the mean value for each bin. Because the UT was approximately equal to the MLT at the Syowa station, we could obtain the mean values of electron fluxes by selecting the bins whose UT and MLT values were equal.

References

Baker, D. N., C. A. Barth, K. E. Mankoff, S. G. Kanekal, S. M. Bailey, G. M. Mason, and J. E. Mazur (2001), Relationships between precipitating auroral zone electrons and lower thermospheric nitric oxide densities: 1998–2000, *J. Geophys. Res.*, *106*(A11), 24,465–24,480, doi:2001JA000078.

Barth, C. A., K. D. Mankoff, S. M. Bailey, and S. C. Solomon (2003), Global observations of nitric oxide in the thermosphere, *J. Geophys. Res.*, *108*(A1), 1027, doi:10.1029/2002JA009458.

Brasseur, G. P., and S. Solomon (2005), *Aeronomy of the Middle Atmosphere*, 3rd ed., Springer, Dordrecht, Netherlands.

Clilverd, M. A., A. Seppälä, C. J. Rodger, N. R. Thomson, J. Lichtenberger, and P. Steinbach (2007), Temporal variability of the descent of high-altitude NOX inferred from ionospheric data, *J. Geophys. Res.*, *112*(A09307), doi:10.1029/2006JA012085.

Daae, M., P. Espy, H. N. Tyssøy, D. Newnham, J. Stadsnes, and F. Søraas (2012), The effect of energetic electron precipitation on middle mesospheric night-time ozone during and after a moderate geomagnetic storm, Geophys. Res. Lett., 39, L21811, doi:10.1029/2012GL053787.

Evans, D. S., and M. S. Greer (2000), *Polar Orbiting Environmental Satellite Space Environment Monitor-2: Instrument Descriptions and Archive Data Documentation*, NOAA Boulder, Colo.

Fuller‐Rowell, T. J. (1993), Modeling the solar cycle change in nitric oxide in the thermosphere and upper mesosphere, *J. Geophys. Res.*, *98*(A2), 1559–1570.

Gustincic, J.J. (1977), A Quasi-Optical Receiver Design, *Microwave Symposium Digest, 1977 IEEE MTT-S International*, 99-102, doi:10.1109/MWSYM.1977.1124373

Horne, R. B., M. M. Lam, and J. C. Green (2009), Energetic electron precipitation from the outer radiation belt during geomagnetic storms, *Geophys. Res. Lett.*, *36*, L19104, doi:10.1029/2009GL040236.

Jackman, C. H., R. D. McPeters, G. J. Labow, E. L. Fleming, C. J. Praderas, and J. M. Russell (2001), Northern Hemisphere atmospheric effects due to the July 2000 solar proton event, *Geophys. Res. Lett.*, *28*(15), 2883–2886.

Jackman, C. H., M. T. DeLand, G. J. Labow, E. L. Fleming, D. K. Weisenstein, M. K. W. Ko, M. Sinnhuber, and J. M. Russell (2005), Neutral atmospheric influences of the solar proton events in October–November 2003, *J. Geophys. Res.*, *110*, A09S27, doi:10.1029/2004JA010888.

Jackman, C. H. et al. (2011), Northern Hemisphere atmospheric influence of the solar proton events and ground level enhancement in January 2005, *Atmos. Chem. Phys.*, *11*, 6153–6166, doi:10.5194/acp-11-6153-2011.

Jackman, C. H., C. E. Randall, V. L. Harvey, S. Wang, E. L. Fleming, M. López-Puertas, B. Funke, and P. F. Bernath (2013), Middle atmospheric changes caused by the January and March 2012 solar proton events, *Atmos. Chem. Phys. Discuss.*, *13*, 23251–23293, doi:10.5194/acpd-13-23251-2013.

Janssen, M.A., (1993), *Atmospheric Remote Sensing By Microwave Radiometry*, Johm Wiley, New York

Lam, M. M., R. B. Horne, N. P. Meredith, S. A. Glauert, T. Moffat-Griffin, and J. C. Green (2010), Origin of energetic electron precipitation >30 keV into the atmosphere, *J. Geophys. Res.*, *115*, A00F08, doi:10.1029/2009JA014619.

Livesey, N. J., W. V. Snyder, W. G. Read, and P. A. Wagner (2006), Retrieval Algorithms for the EOS Microwave Limb Sounder (MLS), *IEEE Trans. Geosci. Remote Sens.*, *44*(5), 1144–1155, doi:10.1109/TGRS.2006.872327.

Livesey, N. J., W. G. Read, L. Froidevaux, A. Lambert, G. L. Manney, H. C. Pumphrey, M. L. Santee, M. J. Schwartz, S. Wang, R. E. Cofeld, D. T. Cuddy, R. A. Fuller, R. F. Jarnot, J. H. Jiang, B. W. Knosp, P. C. Stek, P. A. Wagner, and D. L. Wu. (2011), Version 3.3 level 2 data quality and description document, http://mls.jpl.nasa.gov/data/v3-3_data_quality_document.pdf

López-Puertas, M., B. Funke, S. Gil-López, T. von Clarmann, G. P. Stiller, M. Höpfner, S. Kellmann, H. Fischer, and C. H. Jackman (2005), Observation of NOx enhancement and ozone depletion in the Northern and Southern Hemispheres after the October–November 2003 solar proton events, *J. Geophys. Res.*, *110*(A9), A09S43, doi:10.1029/2005JA011050.

Maier, D. et al. (2001), European Minor Constituent Radiometer: a new millimeter wave receiver for atmospheric research, *International Journal of Infrared and Millimeter Waves*, *22*(11).

Miyoshi, Y., and R. Kataoka (2005), Ring current ions and radiation belt electrons during geomagnetic storms driven by coronal mass ejections and corotating interaction regions, *Geophys. Res. Lett.*, *32*, L21105, doi:10.1029/2005GL024590.

Miyoshi, Y., K. Sakaguchi, K. Shiokawa, D. Evans, J. Albert, M. Connors, and V. Jordanova (2008), Precipitation of radiation belt electrons by EMIC waves, observed from ground and space, *Geophys. Res. Lett.*, *35*, L23101, doi:10.1029/2008GL035727.

Miyoshi, Y., R. Kataoka, Y. Kasahara, A. Kumamoto, T. Nagai, and M. F. Thomsen (2013), High-speed solar wind with southward interplanetary magnetic field causes relativistic electron flux enhancement of the outer

radiation belt via enhanced condition of whistler waves, *Geophys. Res. Lett.*, *40*, 4520–4525, doi:10.1002/grl.50916, 2013.

Mizuno, A., T. Nagahama, A. Morihira, H. Ogawa, N. Mizuno, Y. Yonekura, H. Yamamoto, H. Nakane, and Y. Fukui (2002), Millimeter-wave radiometer for the measurement of stratospheric ClO using a superconductive (SIS) receiver installed in the southern hemisphere, *Int. J. Infrared Milli.*, *23*(981-995), doi:10.1023/A:1019618917005, 2002.

Nagahama, T., H. Nakane, Y. Fujinuma, M. Ninomiya, H. Ogawa, and Y. Fukui (1999), Ground-based millimeter-wave observations of ozone in the upper stratosphere and mesosphere over Tsukuba, *Earth Planets Space, 51*, 1287–1296.

Newnham, D. A., P. J. Espy, M. A. Clilverd, C. J. Rodger, A. Seppälä, D. J. Maxfield, P. Hartogh, K. Holmén, and R. B. Horne (2011), Direct observations of nitric oxide produced by energetic electron precipitation into the Antarctic middle atmosphere, *Geophys. Res. Lett.*, *38*, L20104, doi:10.1029/2011GL048666.

Newnham, D. A., P. J. Espy, M. A. Clilverd, C. J. Rodger, A. Seppälä, D. J. Maxfield, P. Hartogh, C. Straub, K. Holmén, and R. B. Horne (2013), Observations of nitric oxide in the Antarctic middle atmosphere during recurrent geomagnetic storms, *J. Geophys. Res.*, *118*, 1–12, doi:10.1002/2013JA019056.

Ogawa, T., and T. Shimazaki (1975), Diurnal variations of odd nitrogen and ionic densities in the mesosphere and lower thermosphere: Simultaneous solution of photochemical-diffusive equations, *J. Geophys. Res.*, *28*, 28.

Parrish, A., R. L. deZafra, P. M. Solomon, and J. W. Barrett (1988), A ground-based technique for millimeter wave spectroscopic observations of stratospheric trace constituents, *Radio Science*, *23*, 106–118.

Pickett, H. M., R. L. Poynter, E. A. Cohen, M. L. Delitsky, J. C. Pearson, and H. S. . Müller (1998), Submillimeter, millimeter, and microwave spectral line catalog, *J. Quant. Spectrosc. Radiat.Transfer*, *60*(5), 883–890.

Randall, C. E., D. E. Siskind, and R. M. Bevilacqua (2001), Stratospheric NO_x enhancements in the southern hemisphere vortex in winter/spring of 2000, *Geophys. Res. Lett.*, *28*(12), 2385–2388.

Randall, C. E., V. L. Harvey, C. S. Singleton, S. M. Bailey, P. F. Bernath, M. Codrescu, H. Nakajima, and J. M. Russell (2007), Energetic particle precipitation effects on the Southern Hemisphere stratosphere in 1992–2005, *J. Geophys. Res.*, *112*(D8), D08308, doi:10.1029/2006JD007696.

Randall, C. E., V. L. Harvey, D. E. Siskind, J. France, P. F. Bernath, C. D. Boone, and K. A. Walker (2009), NOx descent in the Arctic middle atmosphere in early 2009, Geophys. Res. Lett., 36, L18811, doi:10.1029/2009GL039706.

Rodger, C. J., M. A. Clilverd, J. C. Green, and M. M. Lam (2010), Use of POES SEM-2 observations to examine radiation belt dynamics and energetic electron precipitation into the atmosphere, *J. Geophys. Res.*, *115*, A04202, doi:10.1029/2008JA014023, 2010.

Sato, K., M. Tsutsumi, T. Sato, T. Nakamura, A. Saito, Y. Tomikawa, K. Nishimura, M. Kohma, H. Yamagishi, and T. Yamanouchi (2013), Program of the Antarctic Syowa MST/IS Radar (PANSY), *J. Atmos. Sol. Terr. Phys.*, doi:10.1016/j.jastp.2013.08.022, in press

Schoeberl, M. R. et al. (2006), Overview of the EOS Aura Mission, *IEEE Trans. Geosci. Remote Sens.*, *44*(5), doi:10.1109/TGRS.2005.861950.

Seppälä, A., P. T. Verronen, V. Sofieva, J. Tamminen, E. Kyrölä, C. J. Rodger, and M. A. Clilverd (2006), Destruction of the tertiary ozone maximum

during a solar proton event, *Geophys. Res. Lett.*, *33*, L07804, doi:10.1029/2005GL025571.

Seppälä, A., P. T. Verronen, M. A. Clilverd, C. E. Randall, J. Tamminen, V. Sofieva, L. Backman, and E. Kyrölä (2007), Arctic and Antarctic polar winter NOx and energetic particle precipitation in 2002–2006, *Geophys. Res. Lett.*, *34*(12), L12810, doi:10.1029/2007GL029733.

Sheese, P. E., R. L. Gattinger, E. J. Llewellyn, C. D. Boone, and K. Strong (2011), Nighttime nitric oxide densities in the Southern Hemisphere mesosphere–lower thermosphere, *Geophys. Res. Lett.*, *38*, L15812, doi:10.1029/2011GL048054.

Sinnhuber, M., H. Nieder, and N. Wieters (2012), Energetic Particle Precipitation and the Chemistry of the Mesosphere/Lower Thermosphere, *Surveys in Geophysics*, *33*, 1281–1334, doi:10.1007/s10712-012-9201-3.

Siskind, D. E., and J. M. Russell III (1996), Coupling between middle and upper atmospheric NO: Constraints from HALOE observations, *Geophys. Res. Lett.*, *23*(2), 137–140.

Smith, A. K., R. R. Garcia, D. R. Marsh, and J. H. Richter (2011), WACCM simulations of the mean circulation and trace species transport in the winter mesosphere, *J. Geophys. Res.*, *116*, D20115, doi:10.1029/2011JD016083.

Solomon, S. C., C. A. Barth, and S.M. Bailey (1999), Auroral production of nitric oxide measured by the SNOE satellite, *Geophys. Res. Lett.*, *26*(9), 1259–1262, doi:1999GL900235.

Suzuki, H., T. Nakamura, M. K. Ejiri, M. Abo, T. D. Kawahara, Y. Tomikawa, and M. Tsutsumi (25-29 June 2012), RAYLEIGH RAMAN LIDAR SYSTEM CAPABLE FOR TROPOSPHERIC TO MESOSPHERIC OBSERVATION AT SYOWA STATION, ANTARCTICA., ILRC 26, ICLAS,Greece

Tsutsumi, M., T. Aso, and M. Ejiri (2001), Initial results of Syowa MF radar observations in Antarctica, *Adv. Polar Upper Atmos. Res*, *15*, 103–116.

Tucker, J. R., and M. J. Feldman (1985), Quantum detection at millimeter wavelengths, *Reviews of Modern Physics*, *57*, 1055–1113, doi:10.1103/RevModPhys.57.1055, 1985.

Turunen, E., P. Verronen, A. Seppälä, C. J. Rodger, M. A. Clilverd, J. Tamminen, C.-F. Enell, and T. Ulich (2009), Impact of different energies of precipitating particles on NO_x generation in the middle and upper atmosphere during geomagnetic storms, *J. Atmos. Sol.Terr. Phys.*, *71*, 1176–1189, doi:10.1016/j.jastp.2008.07.005.

Ulich, B., J. H. Davis, P. Rhodes, and J. Hollis (1980), Absolute brightness temperature measurements at 3.5-mm wavelength, *Antennas and Propagation, IEEE Transactions on* , 28, 3, 367-377, doi: 10.1109/TAP.1980.1142330

Verronen, P. T., A. Seppälä, M. A. Clilverd, C. J. Rodger, E. Kyrölä, C.-F. Enell, T. Ulich, and E. Turunen (2005), Diurnal variation of ozone depletion during the October–November 2003 solar proton events, *J. Geophys. Res.*, *110*, A09S32, doi:10.1029/2004JA010932, 2005.